

HIGH-RESOLUTION RADAR BACKSCATTER FROM SEA ICE  
AND  
RANGE-GATED STEP-FREQUENCY RADAR USING THE FM-CW  
CONCEPT

by

Pannirselvam Kanagaratnam  
B.S.E.E., University of Kansas, 1993

Submitted to the Department of Electrical  
Engineering and Computer Science and the  
Faculty of the Graduate School of The  
University of Kansas in partial fulfillment of the  
requirements for the degree of Master of  
Science

---

Professor in Charge

---

Committee Members

Date Defended: December 4, 1995

*To my parents*

## Table of Contents

List of Figures .....	v
List of Tables .....	ix
Acknowledgements .....	x
Abstract.....	xi
<b>Part I - High-Resolution Radar Backscatter From Sea Ice.....</b>	<b>1</b>
<b>Chapter 1 – Introduction.....</b>	<b>2</b>
1.1 Why Remote Sensing of Sea Ice ? .....	2
1.2 Evolution of Sea Ice Research Using Scatterometers .....	4
1.3 Why Broad-Band and Dielectric Measurements Are Needed.....	5
1.4 Organization.....	8
<b>Chapter 2 - The Plane-Wave System.....</b>	<b>9</b>
2.1 Principles of Plane-Wave Illumination .....	10
2.2 Step-Frequency Radar .....	13
2.2.1 Principles of Operation of The Step-Frequency Radar .....	13
<b>Chapter 3 - US Army Cold Regions Research and Engineering Laboratory     Experiment (CRRELEX) Description .....</b>	<b>19</b>
<b>Chapter 4 - Signal Processing of the Ultra-Wide-Band Radar Data .....</b>	<b>22</b>
4.1 Introduction.....	22
4.2 Signal Processing.....	26
4.3 Calibration.....	34
<b>Chapter 5 - Scattering Theory .....</b>	<b>37</b>

<b>Chapter 6 - CRRELEX Results .....</b>	<b>41</b>
6.1 Impulse Response .....	41
6.2 Angular Scattering Response .....	44
6.3 Frequency Scattering Response .....	48
<b>Chapter 7 - Conclusions and Future Work .....</b>	<b>51</b>
<b>Part II - Range-Gated Step-Frequency Radar Using the FM-CW Concept .....</b>	<b>53</b>
<b>Chapter 8 - Range-Gated Step-Frequency Radar .....</b>	<b>54</b>
8.1 Introduction .....	54
8.2 Principles of Operation .....	55
8.2.1 Principles of FM-CW Radar Operation .....	55
8.2.2 Principles of Operation of the Range-Gated Step-Frequency Radar.....	58
8.3 Simulation .....	61
8.4 System Description .....	65
8.4.1 Sawtooth Waveform Generator .....	66
8.4.2 FM Driver .....	67
8.4.3 RF Section.....	70
8.4.4 IF Section .....	74
8.4.5 Data Acquisition .....	76
8.5 Systems Test .....	79
8.6 Conclusions and Future Work .....	87
<b>References .....</b>	<b>89</b>
<b>Bibliography .....</b>	<b>94</b>

## List of Figures

<b>Figure 2.1</b> (a) Conventional radar systems. (b) Plane wave system.....	9
<b>Figure 2.2</b> Geometry of Parabolic Reflector .....	11
<b>Figure 2.3(a)</b> Field of plane wave 6 feet away from the antenna shown for 1994 System.....	12
<b>Figure 2.3(b)</b> Field of plane wave 6 feet away from the antenna shown for 1995 System.....	12
<b>Figure 2.4</b> Block diagram of network-analyzer based step-frequency radar .....	17
<b>Figure 2.5</b> Setup of the UWB radar-compact range antenna system .....	18
<b>Figure 4.1(a)</b> Horizontal distance used for illuminated area calculation in 1994 .....	23
<b>Figure 4.1(b)</b> Vertical distance used for illuminated area calculation in 1994 .....	24
<b>Figure 4.1(c)</b> Horizontal distance used for illuminated area calculation in 1995 .....	24
<b>Figure 4.1(d)</b> Vertical distance used for illuminated area calculation in 1995 .....	25
<b>Figure 4.2</b> Data processing steps to extract frequency response of return from ice....	26
<b>Figure 4.3</b> Raw step-frequency radar data.....	27
<b>Figure 4.4</b> Windowed data .....	27
<b>Figure 4.5</b> Impulse response of windowed and zero-padded data .....	28
<b>Figure 4.6</b> Result of CNR on pancake ice at 15° incidence angle. These data were collected using the plane-wave system during the CRRELEX '95 experiment.....	29
<b>Figure 4.7</b> Isolating return from ice .....	30
<b>Figure 4.8</b> Frequency response of data filtered with a rectangular filter.....	31
<b>Figure 4.9(a)</b> Frequency response of filtered data using Gaussian filter .....	32

<b>Figure 4.9(b)</b> Frequency response of data filtered with a Gaussian filter with correction factor applied.....	33
<b>Figure 4.10</b> Uncalibrated return power as a function of frequency for pancake ice at $0^\circ$ .....	34
<b>Figure 4.11</b> Theoretical scattering response of an 8-inch-diameter sphere.....	35
<b>Figure 4.12</b> Ideal impulse response for an 8-inch metal sphere.....	35
<b>Figure 4.13</b> Measured impulse response of sphere .....	36
<b>Figure 5.1(a)</b> Typical surface scattering pattern .....	37
<b>Figure 5.1(b)</b> Typical volume scattering pattern.....	38
<b>Figure 5.2 (a)</b> Example of a primarily coherent return from pancake ice at $0^\circ$ .....	39
<b>Figure 5.2 (b)</b> Example of a primarily incoherent return from pancake ice at $15^\circ$ .....	39
<b>Figure 6.1</b> Return from bare ice at $0^\circ$ .....	41
<b>Figure 6.2</b> Return from bare ice at $0^\circ$ and $5^\circ$ .....	42
<b>Figure 6.3</b> Return from snow-covered ice at $0^\circ$ .....	42
<b>Figure 6.4</b> Comparison of backscattering coefficient from bare ice obtained using plane-wave and spherical-wave antennas at Ku band.....	45
<b>Figure 6.5</b> Angular response of bare ice, snow-covered ice and pancake ice at C band .....	46
<b>Figure 6.6</b> Angular response of bare ice, snow covered ice and pancake ice at Ku band.....	46
<b>Figure 6.7</b> Comparison between field and laboratory measurement of pancake ice .....	47
<b>Figure 6.8</b> Frequency response of bare ice, snow-covered ice and pancake ice at $0^\circ$ .....	49

<b>Figure 6.9</b> Frequency response of bare ice, snow-covered ice and pancake ice at 5° .....	49
<b>Figure 6.10</b> Frequency response of bare ice, snow covered ice and pancake ice at 20° .....	50
<b>Figure 8.1</b> Transmit and receive signal from a point target for a FM-CW radar .....	56
<b>Figure 8.2</b> Processing steps for the range-gated step-frequency radar .....	60
<b>Figure 8.3</b> Single target simulated at 5m .....	61
<b>Figure 8.4</b> Two targets simulated at 5m and 5.05m, respectively.....	62
<b>Figure 8.5</b> Single target simulated at 20m .....	63
<b>Figure 8.6</b> Comparison in system performance when oscillator's frequency is swept the entire frequency span (2-18 GHz) and when it is swept in the linear region of operation (2.37 - 17.65 GHz).....	64
<b>Figure 8.7</b> Block diagram of the range-gated step-frequency radar .....	65
<b>Figure 8.8</b> Circuit layout of FM driver.....	68
<b>Figure 8.9</b> (a) FM driver's input waveform. (b) FM driver's output waveform .....	70
<b>Figure 8.10</b> Measured stepsize of oscillator's frequency .....	72
<b>Figure 8.11</b> Drift in oscillator's frequency.....	72
<b>Figure 8.12</b> Block diagram of IF section.....	75
<b>Figure 8.13</b> Component layout of the range-gated step-frequency radar .....	77
<b>Figure 8.14</b> Front and back panel of the radar/probe .....	78
<b>Figure 8.15</b> Configuration of the monopole antenna .....	80
<b>Figure 8.16 (a)</b> Real part of input impedance .....	81
<b>Figure 8.16 (b)</b> Imaginary part of input impedance .....	81

<b>Figure 8.17 (a)</b> Magnitude of reflection coefficient of open load.....	85
<b>Figure 8.17 (b)</b> Phase of reflection coefficient of open load .....	85
<b>Figure 8.18</b> Measured permittivity of rubber. Theoretical permittivity of rubber is 3 for the real part and 0 for the imaginary part .....	86
<b>Figure 8.19</b> Result of delay line measurement with 0-dB gain .....	87

## List of Tables

<b>Table 3.1</b> CRRELEX '94 January Data Summary .....	20
<b>Table 3.2</b> CRRELEX '94 March Data Summary .....	21
<b>Table 3.3</b> CRRELEX'95 Data Summary .....	21
<b>Table 8.1</b> FM-CW Radar Parameters .....	66

## **Acknowledgments**

I am very grateful to **Dr. Sivaprasad Gogineni** for giving me the opportunity to do research in the field of radar design, signal processing and sea ice remote sensing. He has spent countless hours, days and nights even during the weekends helping me whenever I ran into problems. I am thankful to him for the extensive knowledge that I have gained by working with him for the last three years.

I would also like to extend my thanks to the following people for the help that they have provided during the course of my studies.

**Dr. Swapan Chakrabarti** - for helping me with signal processing problems

**Dr. Glenn Prescott** - for serving on my MS committee

**Dr. Scott Beaven** - for being patient in explaining many of the concepts in radars and sea ice remote sensing

**Donnis Graham** - for editing this thesis

**Wes Ellison** - for assembling the radar

**Glenn Waterfield** - for letting me borrow the calibration kit and making the probe

**Lance Lockhart** - for the IF Amplifiers and help editing this thesis

**Reza Hossienmostafa** - for introducing me to the field of sea ice remote sensing

**Lou Brown** - for making me many of those hard-to-make RF cables

**Chuah Teong Sek & Justin Legarsky** - for helping me with the PCB layout

**Efugbaike Ajayi & Alfiya Vali** - for helping me with the data processing

**Mohan Kambhammettu** - for helping me with Matlab and Latex problems

## **Abstract**

An ultra-wideband radar and a plane-wave antenna have been used to measure the high resolution scattering response of bare saline ice, snow-covered ice and pancake ice during the winter season at the US Army Cold Regions Research and Engineering Laboratory (CRREL) during the 1994 and 1995 winter seasons. We have developed signal processing techniques to extract the wideband response of a signal using narrowband filters in the spectral domain. We have shown how the droop associated with narrowband filters can be reduced by using a correction factor. The results of our measurements show the excellent spatial and angular resolution that can be achieved with the plane wave system. The scattering coefficients obtained using the plane-wave system show that surface scattering dominates at least until  $30^\circ$ . At  $0^\circ$ , the scattering from bare ice stayed fairly constant with about 1-2 dB variation across the 5-18 GHz frequency range, while the scattering from pancake ice increased from 16 to 27 dB with increasing frequency. On the other hand, the scattering from snow-covered ice decreased from 24 to 15 dB with increasing frequency. This shows that there is more contribution from incoherent components for pancake ice at the higher frequencies, while for the snow-covered ice there is less contribution from the coherent component at the higher frequencies. At incidence angles other than  $0^\circ$ , the scattering increased as a function of frequency, which is an indication of dominant incoherent scattering. With increasing incidence angle, the scattering level dropped. This is an indication of dominant surface scattering. Field measurement of pancake ice at  $35^\circ$  shows agreement with laboratory measurements at the lower bound.

A range-gated step-frequency radar has been developed using the FM-CW concept for the purpose of measuring relative permittivity of materials and scattering from geophysical surfaces. The radar operates from 2.37-17.65 GHz and is capable of being operated in either monostatic and bistatic mode. The radar has the high resolution of a step-frequency radar and the range-gating capability of the FMCW radar. The radar has a wide range of applications including high-resolution probing of geophysical surfaces and ground-penetration applications.

**PART I**

**HIGH-RESOLUTION RADAR BACKSCATTER**

**FROM SEA ICE**

# **Chapter 1**

## **Introduction**

### **1.1 Why Remote Sensing of Sea Ice ?**

Remote sensing is the measurement of properties of an object without contact with it. Remote sensing is the only effective way to obtain data on a global scale so the scientific community may understand better how the Earth functions and how human activities affect it. It can be used to study, among other things, climatic changes, pollution and land use. One such area of interest is the study of sea ice and its role in the climate system.

About 10% of the ocean is covered by sea ice. Remote sensing of these areas has been the subject of extensive research due to their importance in global change and operational activities including shipping in the polar regions, offshore operations in the marginal seas and harbor operations [Carsey et al., 1992].

Sea ice modulates energy exchange between the ocean and the atmosphere. Sea ice thickness determines the amounts of energy exchange between the air and the ocean. The thicker the ice cover, the more effective is the insulation between the cold polar air and the warm ocean. Heat flux through open water is about 100 times that through thick ice. Even thin ice (<30 cm), which is the primary focus of our experiments, can reduce the heat flux considerably.

Sea ice also plays an important role in the surface radiation budget. Because of its high albedo, sea ice can reflect up to 90% of the solar radiation. On the other hand,

the open ocean absorbs most of the solar energy (85 - 90%) due to its low albedo. Consequently, the changes in sea ice extent over time can be an indicator of the energy being retained by the Earth. A negative change in the sea ice extent would indicate a global warming scenario.

The ice cover also serves as a seasonal buffer between the atmosphere and ocean. In the winter, the growing ice releases brine into the ocean. The cold dense brine sinks into the ocean resulting in convective overturning, which causes the heat to be transported to the surface where it is rapidly lost to the ice. In summer, the melting ice contributes to the fresh water surface layer, which affects deep water convection. The presence of sea ice also affects the biological activities in the ocean since it absorbs most of the solar radiation, which is a vital requirement for marine life.

It is also important for us to be able to distinguish between different ice ages, particularly first-year and multiyear ice. This is especially important in navigation since multiyear ice is usually more dangerous to ships than first-year ice because of its greater thickness and the fact that it also has more ridges.

Thus it is essential that our planet's sea ice is monitored on a global scale. The only way we can achieve this is by remote sensing from satellites. Because of these reasons and the capability of active microwave sensors to characterize sea ice, the radar backscatter signatures of the sea ice are of intensive research interest.

## **1.2 Evolution of Sea Ice Research Using Scatterometers**

The first scattering measurement from sea ice was made in 1956, at Thule, Greenland, by the Naval Research Laboratory using a 0.4- and 10-GHz radar [Onstott, 1992]. Radar imaging of sea ice was first attempted by the US Army Cold Regions Research and Engineering Laboratory. The result showed that first-year and multiyear ice could be distinguished using side-looking radar (SLAR) images [Anderson, 1966].

Quantitative measurements of sea ice began with Rouse's [1969] experiments over the Beaufort Sea using a 13.3-GHz scatterometer. This was the first time a correlation was made between ice type and the backscattering coefficient. Parashar et al.[1977] extended this study by comparing backscatter measurements made at 400 MHz and 13.3 GHz with 15-GHz images. Ice type classification at 15 GHz using a combination of angular dependence of scattering and the magnitude of the scattering was first suggested by Gray et al. [1977].

To understand better the scattering mechanisms from sea ice, The University of Kansas began in situ scatterometer measurements on sea ice, the first of its kind. This was done in 1977, at Pt. Barrow, Alaska, using L-, X- and Ku-band scatterometers. Thus began extensive on-site experiments at various locations including the Labrador Sea, Mould Bay, and many others. These measurements have been analyzed, and the results of scattering from various ice types during the various seasons have been documented. In summary, the important results that are discovered by these experiments were that backscatter from first-year ice (FYI) was dominated by surface scattering and backscatter from multiyear ice (MYI) was dominated by volume scattering. It was also

found that backscatter from FYI and MYI could not be distinguished during the summer. The nature of backscatter from the ice was found to be governed by two major factors, the relative permittivity and the physical properties of the medium such as surface roughness, temperature and salinity.

In the early 80s experiments were made to study the seasonal effects of sea ice on the microwave signatures. Measurements made at Mould Bay indicated that there was significant variation in the backscatter due to the presence of melt water [Gogineni, 1984; Onstott and Gogineni, 1985]. The microwave signatures from early melt through advance melt have been characterized by Livingstone et al. [1987]. Measurements made using synthetic aperture radar (SAR) at several frequencies during the Marginal Ice Zone Experiment (MIZEX) in the Fram Strait during the summer of 1984, showed the difficulty in distinguishing multiyear and first-year ice during the summer [Onstott et al., 1987]. The microwave signatures of sea ice during the fall freeze-up to the onset of melt were studied during the Coordinated Eastern Arctic Research Experiment (CEAREX) from September 1988 to March 1989 [Onstott and Shuchman, 1990]. Similar measurements were also made at C band by Beaven and Gogineni [1994].

### **1.3 Why Broad-Band and Dielectric Measurements Are Needed**

Broad-band measurements enable us to perform high-resolution probing. This comes from Fourier transform theory, which defines the inverse relationship between the frequency domain and time domain: the wider the sweep bandwidth, the higher the time resolution, hence better resolving capabilities. Broad-band measurements also

provide a convenient means of studying the scattering characteristics of sea ice and provide a vigorous test for models at many frequencies using a single system instead of many single-frequency systems.

As stated in Section 1.2, the relative permittivity of sea ice is a major factor in determining its backscattering characteristics. The relative permittivity is a complex number that characterizes the electrical properties of the material. The relative permittivity is given by

$$\epsilon = \epsilon' - j\epsilon''$$

where  $\epsilon'$  is the dielectric constant of the material with respect to free space.

The dielectric loss factor is  $\epsilon''$ , which is the electromagnetic loss of the material. The real part of the relative permittivity sets the absolute backscatter level. The larger the dielectric constant, the larger the backscattering level. The depth of penetration of electromagnetic (EM) waves into the ice is governed by the imaginary part of the relative permittivity. In sea ice, the dielectric loss factor is determined by the brine content and temperature. The higher the brine content, the higher the imaginary part; hence it is more lossy. FYI has a high brine concentration, the reason why its backscatter has little contribution from the volume.

In order to perform broad-band scattering measurements, we developed a network-analyzer-based ultra-wideband (UWB) radar using a compact range antenna. This system, as well as providing exceptional range resolution, also provides excellent angular resolution because of the plane waves generated by the compact range antenna

[Gogineni et al., 1995]. Previous radar systems using horn antennas had beamwidths in the range of  $6^\circ$  to  $20^\circ$ , which made it difficult to determine the scattering mechanisms from distributed targets as a function of incidence angle. With this high range resolution, on the order of centimeters, we were able to resolve the reflections from the complex ice layers, which was never accomplished before. Measurements were made using this system on artificially grown sea ice at the US Army Cold Regions Research and Engineering Laboratory in the winters of 1994 and 1995 to study the scattering response of young saline ice.

But this system, as with any short-range, single-antenna system, has limitations. In these systems, there are many interference and leakage signals that are usually much higher than those from the return from the target. Antenna reflection, for one, is a primary source of interference that severely limits the sensitivity of the system. Also, there are reflections from mismatches between the RF components. There is additionally the problem of limited isolation when the oscillator signal leaks into the receive path. These signals severely limit the sensitivity of the radar. Range-gating techniques improve the sensitivity of short-range radars by eliminating the reflections up to the point of the antenna reflection. While this technique is easily implemented in short-range FM radars by using high-pass filters to eliminate these unwanted reflections, we have failed to implement the range-gating technique in step-frequency radars because of the fast switches needed to operate at short ranges of 2 - 3m.

In this project, the design and construction of a new range-gated step-frequency radar/probe using the FM-CW concept is presented. This radar is ideal for performing in

situ scattering and relative permittivity measurements of sea ice as opposed to the network analyzer, which is not very portable.

## **1.4 Organization**

This thesis is divided into 8 chapters. In Chapter 2, a description of the plane-wave system and the principles of operation of the step-frequency radar are presented. The descriptions of the experiments performed at CRREL in the winters of 1994 and 1995 are presented in Chapter 3. Angular scattering measurements and probability distribution function (pdf) measurements were made on bare ice and snow-covered ice in the winter of 1994 and on pancake ice in the winter of 1995. The data processing technique using the plane-wave system is presented in Chapter 4. In Chapter 5, we give a brief review on scattering theory related to sea ice. The results of data processing are presented in Chapter 6. Angular and frequency backscatter responses of the various ice types are presented here. A summary and future improvements to the signal processing techniques are given in Chapter 7. In Chapter 8, the design and construction of the range-gated step-frequency radar using the FM-CW concept is presented. The principle of operation of the FM-CW radar is given in this chapter. Also, the theoretical basis of the range-gated step-frequency radar is presented. A description of the monopole antenna used for dielectric measurement is also included in this chapter. And finally a general conclusion and recommendation for improvements on future research are given.

## Chapter 2

### The Plane-Wave System

To obtain better resolving capability and angular response of saline ice we used a compact range antenna with a wideband (2- to 18-GHz) network-analyzer-based radar. Previous radar systems used antennas whose illumination of the distributed target contains a wide range of incidence angles, which makes it difficult to determine primary scattering sources. Figure 2.1 shows a comparison between the plane-wave system and conventional systems.

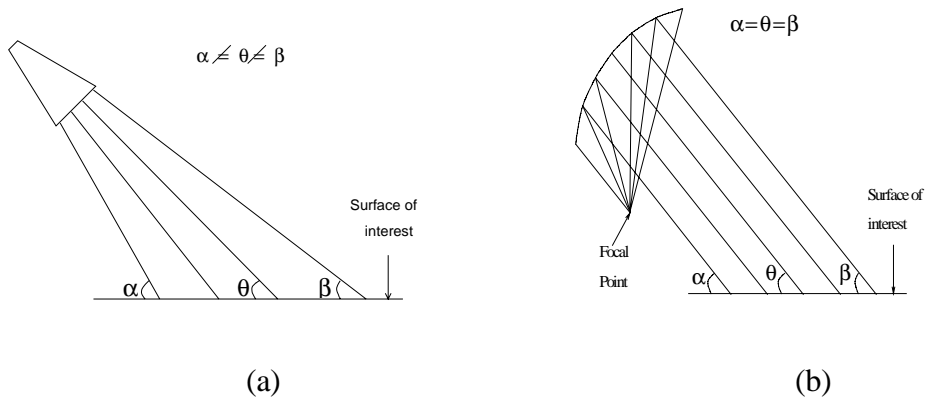


**Figure 2.1** (a) Conventional radar systems. (b) Plane-wave system

A 42-inch-diameter parabolic reflector antenna is used to transform spherical waveforms from the offset AEL horn feed antenna into a plane wave of uniform phase over an area approximately equal to the area of the reflector and at ranges up to  $0.5 \cdot D^2 / \lambda$ , where  $D$  is the reflector diameter and  $\lambda$  is the wavelength. The feed has been adjusted to place the phase center of the feed at the focal point of the reflector. Both

vertically and horizontally polarized measurements can be made with this system by properly orienting the feed. The rims of the reflector and the feed support were covered with echosorb to minimize the distortion of the incident plane wave and to reduce the scattering from these objects.

## **2.1 Principles of Plane-Wave Illumination**

Theory and implementation of compact range antenna is well documented [Pistorius and Burnside, 1987; Kouyoumjian and Pathak, 1974; Ryan and Peters, 1969].

A brief summary of the concept of the compact range antenna is given here.

Plane waves are generated by using a parabolic reflector to convert rays emanating from a spherical source at the focal point to plane waves. Due to the finite nature of the parabolic reflector, the plane-wave is contaminated by diffracted rays from the edges (figure 2.2). The rays, which are diffracted in the region within the reflection boundary (RB), are parallel to the plane-wave. As for the rays diffracted outside the RB region, they are spherical in nature and their amplitude decays by  $1/r$ . Several ways have been investigated to reduce this edge effect, including the use of echosorb, serrated and rolled edges [Jezek et al., 1994]. In the CRREL '95 experiment, echosorb was used to reduce the effects of diffraction from edges.

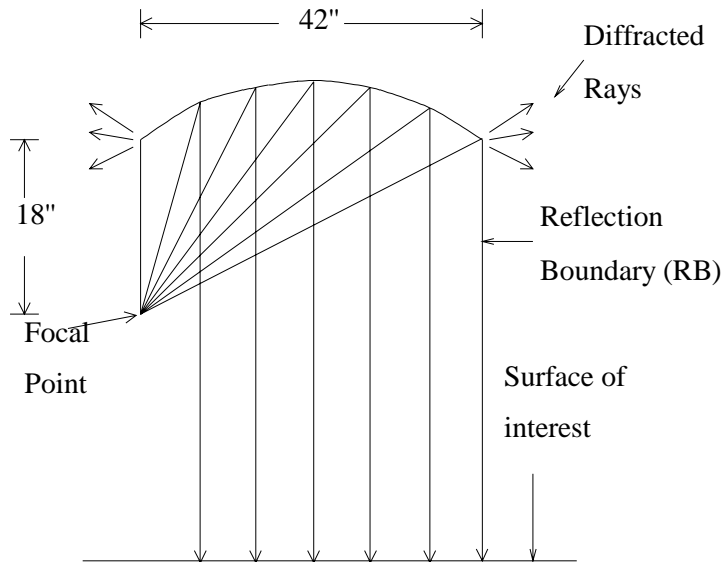


**Figure 2.2** Geometry of parabolic reflector

The size of the antenna is determined by the frequency of operation. Ideally, the reflector should be 10 wavelengths at the lowest frequency to be effective in the compact range, but reasonable results have been shown for reflectors with diameters of 3 to 5 wavelengths [Jezek et al., 1994]. The type of feed used is determined by the bandwidth of operation. The fields from the reflector were probed in both the horizontal and vertical directions in the desired range of operation using a network analyzer. The results at two frequencies for the compact range antenna system used in CRRELEX '94 and '95 are reproduced in figures 2.3(a) and 2.3(b) courtesy of Ellias Nassar. In 1994 the AEL horn feed was used, and in 1995 the transmission line antenna [Nassar, 1992] was used. Notice the improvement in phase response in the 1995 system.

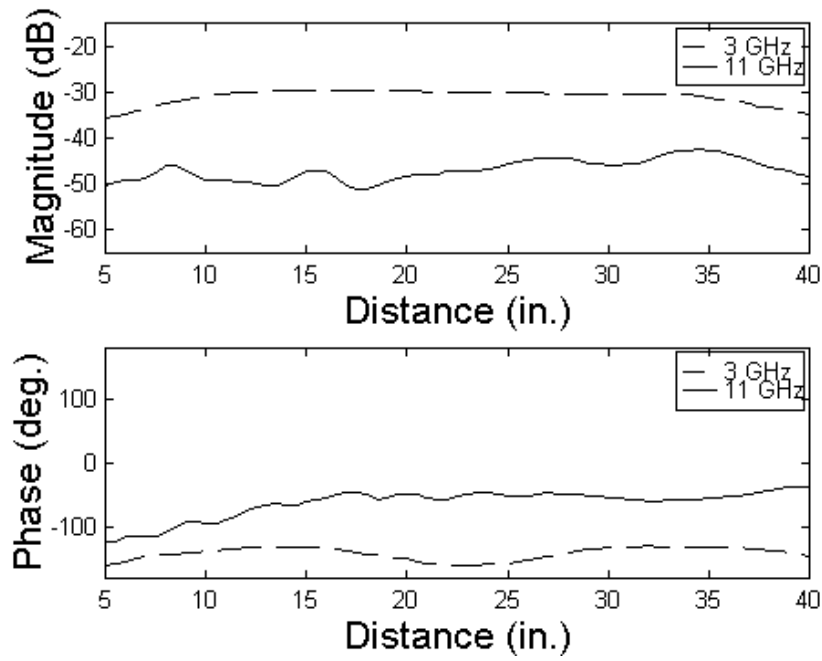


Figure 2.3(a) Field of plane wave 6 feet away from the antenna shown for 1994 system

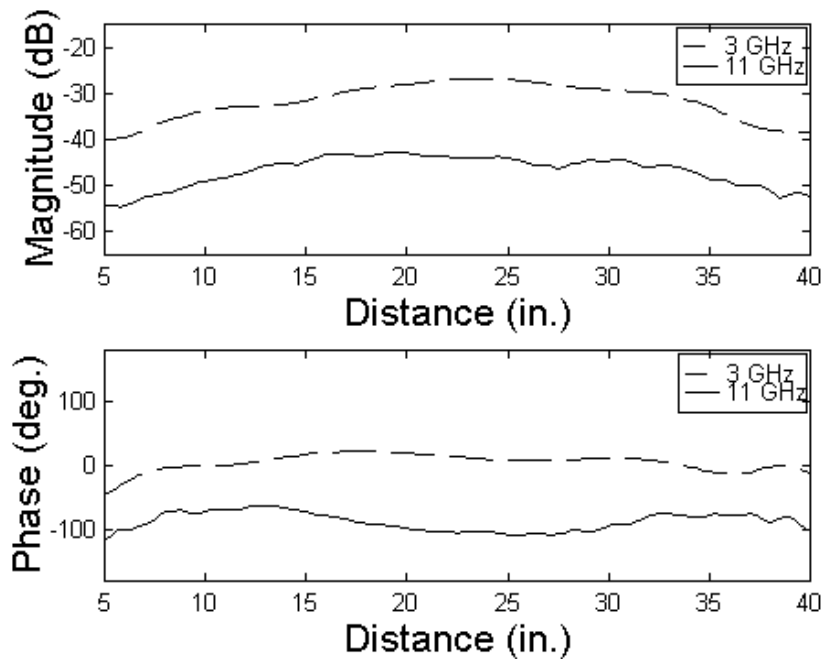


Figure 2.3(b) Field of plane wave 6 feet away from the antenna shown for 1995 system

## 2.2 Step-Frequency Radar

The step-frequency radar [Izuka et al., 1984] was used together with the compact range antenna to measure the scattering coefficient of young saline ice. The main feature of the step-frequency radar is the high resolution that can be obtained by exploiting the phase property of the signal.

### 2.2.1 Principles of Operation of the Step-Frequency Radar

The transmitted step-frequency signal is given by

$$V_t(f) = E_o \quad (2.1)$$

where  $E_o$  is the field strength of the transmit signal.

When this signal travels to a target located at a distance  $d$  from the radar and back, the total number of wavelengths it traveled is equal to

$$N_\lambda = \frac{2d}{\lambda} \quad (2.2a)$$

and the total angular excursion is given by

$$2\pi N_\lambda = 2\beta d \quad (2.2b)$$

where  $\beta$  is the propagation constant ( $2\pi/\lambda$ ).

Assuming that the transmission media is lossless and homogeneous, the return signal for the case of a single point target is then given by

$$V_r(f) = E_o \Gamma \exp(j2\beta d) \quad (2.3)$$

where  $\Gamma$  is the complex reflection coefficient of the target.

The above expression represents the case for a single frequency. When the frequency is increased in uniform steps for N times, we have,

$$V_r(f_n) = E_o \Gamma \exp j(2\beta_n d) \quad (2.4a)$$

and

$$\beta_n = \frac{2\pi f_n}{c} = \frac{2\pi(f_o + n\Delta f)}{c} \quad (2.4b)$$

where  $f_o$  is the start frequency.

The frequency step size is  $\Delta f$  and  $n$  is the frequency step number which is incremented from 0 to N-1.

Expanding  $V_r(f_n)$ , we have

$$V_r(f_n) = E_o \Gamma \exp j\left(\frac{4\pi(f_o + n\Delta f)d}{c}\right) \quad (2.4c)$$

From the above equation, it can be seen that for a fixed  $d$ ,  $V_r(f_n)$  will be sinusoidal with respect to  $n$ , with the period being determined by  $d$ . (Note that this is actually the time series data in the conventional sense. When we talk about the step-frequency radar data in this report, the frequency domain will denote the signal associated with  $V_r(f_n)$ , and the distance (range) or time domain will be associated with the spectrum of  $V_r(f_n)$ ). The Fourier transform of this signal with respect to  $n$  will give us the spectrum of the signal corresponding to the target at location  $d$ , and the distance,  $d$ , can then be easily determined. From the spectrum we can determine the

index location of the target, which we call  $i$ . The relationship between the distance and the index location is simply

$$\frac{2\Delta f d}{c} = \frac{i}{N} \quad (2.5a)$$

$$d = \frac{c}{2\Delta f} \times \frac{i}{N} \quad (2.5b)$$

From the above equations we can define two more important parameters for the step-frequency radar, namely the maximum range and the range resolution ( $\Delta R$ ).

$$\text{Max. Range} = \frac{c}{2\Delta f} \quad (2.6)$$

$$\Delta R = \frac{c}{2\Delta f N} \quad (2.7)$$

We can see from (2.6) that the maximum range for a step-frequency radar is dependent on its frequency step size. The smaller the step size, the larger our maximum range. From (2.7) we can see that for the same step size, we can obtain a higher resolution simply by increasing our sweep bandwidth by increasing the number of steps. In Chapter 8 we will demonstrate how we obtain ranges beyond the maximum defined for a step-frequency radar while maintaining the same resolution.

Now let us consider a typical case where more than one scatterer is present. Lets assume there are  $K$  number of scatterers, from (2.4c),

$$V_r(f_n) = \sum_{k=0}^{K-1} E_{ok} \Gamma_k \exp j \left( \frac{4\pi(f_o + n\Delta f)d_k}{c} \right) \quad (2.8)$$

From (2.8) we can see that for each frequency,  $f_n$ , we have K number of sinusoids with differing periods (assume that no two scatterers are located within the same range resolution,  $\Delta R$ ). In order to resolve all the scatterers we must impose a constraint of having only N number of scatterers. Hence, the maximum value for K is N. The FFT of  $V_r(f_n)$  with respect to n will give us the spectral distribution of all the scatterers with their amplitude and phase given by

$$\text{Amplitude} = E_{ok} |\Gamma_k| \quad (2.9)$$

$$\text{Phase} = \frac{4\pi f_o d_k}{c} + \arg(\Gamma_k) \quad (2.10)$$

The complex reflection coefficient of a target can be determined easily by calibrating the return signal with a target of known reflection coefficient. The complex reflection coefficient as a function of frequency for a target can be obtained simply by centering a bandpass filter over the target of interest and taking the IFFT of the gated signal.

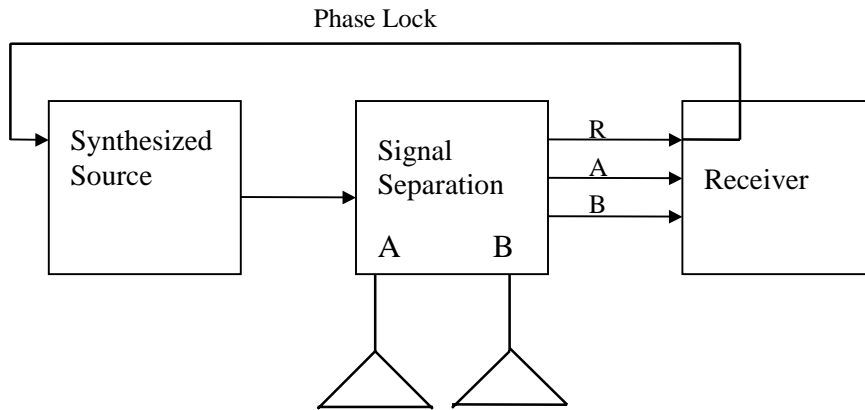


**Figure 2.4** Block diagram of network-analyzer-based step-frequency radar.

The figure above shows a simple block diagram of the network-analyzer-based step-frequency radar used in our experiments. The synthesized source can generate a swept signal in the range of 50 MHz to 40 GHz. The start and stop frequency can be easily selected within this range via software. To achieve high frequency accuracy, a portion of the source signal is routed to the R sampler in the receiver and routed back to the source for phase locking. The signal separation device consists of a power splitter, two directional couplers and a transfer switch. The power splitter couples some of the incident signal to the R sampler for phase locking and reference. The transfer switch is used to switch between measurement in the forward direction ( $S_{11}$  and  $S_{21}$ ) and reverse direction ( $S_{22}$  and  $S_{12}$ ). The directional couplers couple the reflected signal from the target to the A sampler in the receiver for  $S_{11}$  measurement and to the B sampler for  $S_{21}$  measurements when the transfer switch is set in the forward direction. The receiver then downconverts the received signal to IF.

In the experiments that we conducted, the frequency of the network analyzer was stepped through 16 GHz of bandwidth (2-18 GHz in 1994 and 0.5-16.5 GHz in

1995) in 10-MHz steps resulting in 0.94-cm range resolution. Figure 2.5 shows the system configuration of the ultra-wideband (UWB) radar system. Scattering measurements were made in  $S_{11}$  mode with this system at an outdoor saline pond at the CRREL facility in Hanover, New Hampshire.

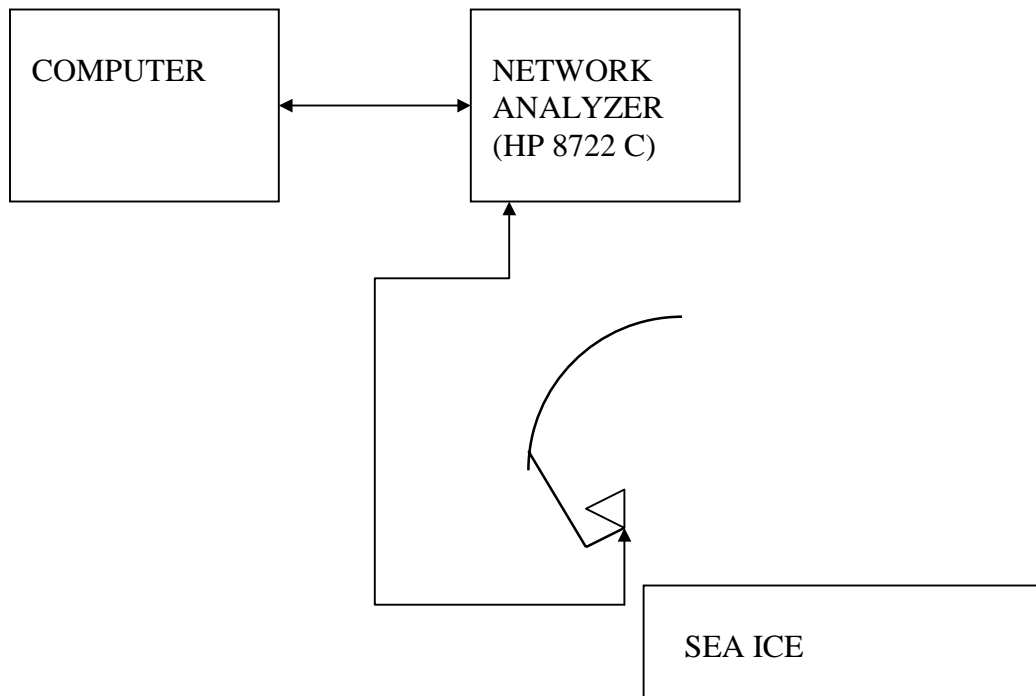


**Figure 2.5** Setup of the UWB radar-compact range antenna system.

## **Chapter 3**

### **US Army Cold Regions Research and Engineering Laboratory Experiment (CRRELEX) Description**

To understand the backscatter mechanisms of sea ice, radar backscatter measurements were performed on artificially grown sea ice in an indoor facility at the US Army Cold Regions Research and Engineering Laboratory (CRREL) during the 1994 and 1995 winter seasons. The frozen pond was made with saline water in order to simulate sea ice. The pond is about 15m wide by 20m long. The facility has a catwalk on railroad tracks that were used to place the antenna mount, the network analyzer and the data acquisition system. The mobility of the catwalk permitted us to obtain four independent samples at each angle and also make 200 independent measurements at a fixed angle for pdf calculations.

In January 1994, measurements were made on bare ice and snow-covered ice at incidence angles ranging from  $0^\circ$  to  $55^\circ$  with VV polarization. Pdf measurements were also made on this ice at nadir. In March 1994, measurements were made on bare ice and snow-covered ice at incidence angles ranging from  $0^\circ$  to  $60^\circ$  with VV and HH polarizations. In January 1995, measurements were made on pancake ice at incidence angles ranging from  $0^\circ$  to  $50^\circ$  with VV and HH polarizations. Pdf measurements were also made on the pancake ice at  $0^\circ$  and  $23^\circ$ . To create pancake ice, waves were generated on open water with a motorized paddle. The wave action caused the formation of frazil ice first, and this slowly grew to pancake ice during freeze-up.

The tables below summarize the measurements made during these experiments.

**Table 3.1** CRRELEX '94 January Data Summary

Date	Angles	Number of Spots	Ice Type	Polarization	Frequency
8 Jan	0°-55°	3	Snow-covered ice	VV	2 - 18 GHz
9 Jan	0°-55°	2	Snow-covered ice	VV	2 - 18 GHz
9 Jan	0°-55°	2	Bare ice	VV	2 - 18 GHz
10 Jan	0°-55°	2	Snow-covered ice	VV	2 - 18 GHz
10 Jan	0°-55°	2	Bare ice	VV	2 - 18 GHz
11 Jan	0°	133 (PDF)	Snow-covered ice	VV	2 - 18 GHz
12 Jan	0°	103 (PDF)	Bare ice	VV	2 - 18 GHz
14 Jan	0°	128 (PDF)	Rough ice	VV	2 - 18 GHz
14 Jan	0°-55°	4	Rough ice	VV	2 - 18 GHz
15 Jan	0°	95 (PDF)	Snow-covered ice	VV	2 - 18 GHz
15 Jan	0°-50°	4	Snow-covered ice	VV	2 - 18 GHz
15 Jan	0°-50°	6	Rough ice	VV	2 - 18 GHz
15 Jan	0°	126 (PDF)	Rough ice	VV	2 - 18 GHz
16 Jan	0°	108 (PDF)	Bare ice	VV	2 - 18 GHz

**Table 3.2** CRRELEX '94 March Data Summary

Date	Angles	Number of Spots	Ice Type	Polarization	Frequency
11 Mar	0° - 60°	4	Snow-covered ice	VV & HH	2 - 18 GHz
12 Mar	0° - 60°	4	Bare ice	VV & HH	2 - 18 GHz

**Table 3.3** CRRELEX'95 Data Summary

Date	Angles	Number of Spots	Ice Type	Pol.	Frequency
5 Jan	0°-50°	4	Bare ice	VV	1 - 16 GHz
7 Jan	0°-40°	4	Snow-covered ice	VV	0.5- 16.5 GHz
8 Jan*	20°	3	Snow-covered ice	VV	0.5- 16.5 GHz
9 Jan*	17°,23°, 31°,41°,44°,50°	1	Bare ice	VV	2 - 18 GHz
10 & 11 Jan	0°-50°	3	Open water to Pancake ice	VV	0.5- 16.5 GHz
23 Jan	0°-50°	4	Pancake ice	VV	0.5- 16.5 GHz
24 Jan	0°	200 (PDF)	Pancake ice	VV	0.5 - 16.5 GHz
25 Jan	0°-50°	4	Pancake ice	VV & HH	0.5 - 16.5 GHz
25 Jan	23°	200 (PDF)	Pancake ice	VV	0.5 - 16.5 GHz

\* Bistatic Measurements

## Chapter 4

### Signal Processing of the Ultra-Wideband Radar Data

#### 4.1 Introduction

The primary parameter to be extracted from our measurements is the backscattering coefficient of the simulated sea ice as a function of the incidence angle and frequency. The radar equation for the plane-wave system is

$$\sigma^o = \frac{P_r \sigma_{cal}}{P_{cal} A_{ill}} \quad (4.1)$$

where  $\sigma^o$  is the backscattering coefficient of the ice,

$P_r$  is the power returned from the ice,

$P_{cal}$  is the return power from a target of known radar cross section,  $\sigma_{cal}$ , and

$A_{ill}$  is the area illuminated by the antenna.

This equation differs from the conventional radar equation because of the absence of range dependence for the plane wave. To compute the illuminated area, we first have to determine the distance between the center of the field (similar to those in figure 2.3) and the point where the magnitude falls off by 6dB for both the horizontal and vertical fields over the frequencies of operation. The distance between the 6-dB points is the distance used in the illuminated area calculations (4.2). The vertical and horizontal fields have been measured in the near-field region (6 ft.) from 1 to 20 GHz in steps of 1 GHz for both vertical and horizontal polarizations at The Ohio State University. The horizontal and the vertical distances in meters are shown in figure 4.1

for the antennas used during the 1994 and 1995 CRREL experiments. The distances have been fitted with a linear fit to interpolate for frequencies at which the patterns were not measured. The vertical diameter for the illuminated area is also modified by the incidence angle. Hence, the illuminated area is

$$A_{ill} = \frac{\pi D_V D_H}{4 \cos(\theta)} \quad (4.2)$$

where  $D_V$  is the vertical distance,

$D_H$  is the horizontal distance, and

$\theta$  is the incidence angle.

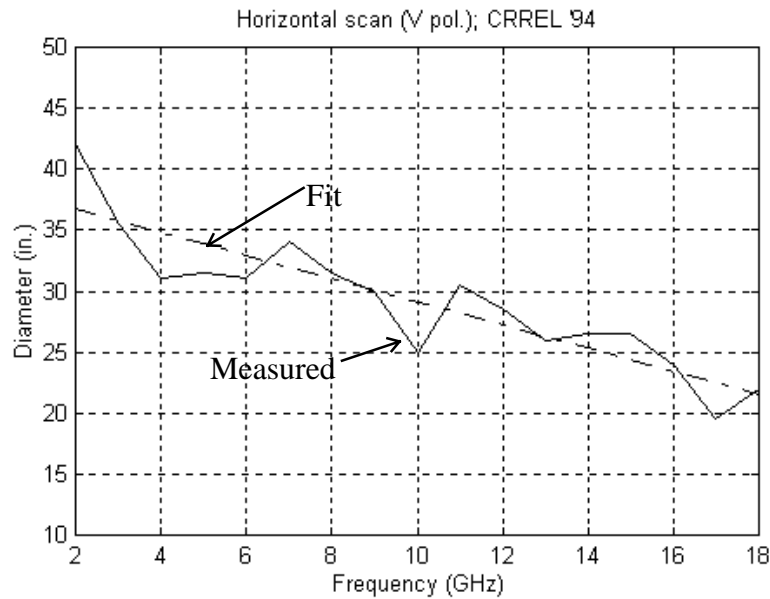


**Figure 4.1(a)** Horizontal distance used for illuminated area calculation in 1994.

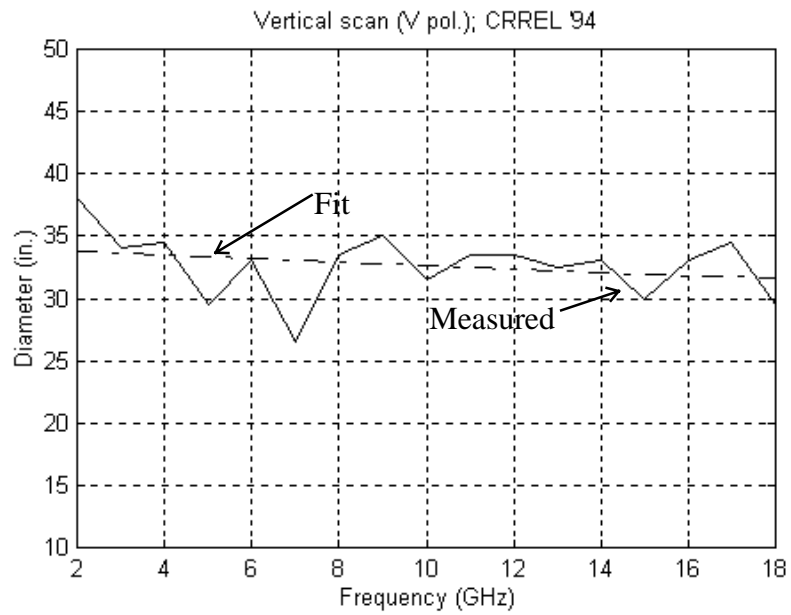


**Figure 4.1(b)** Vertical distance used for illuminated area calculation in 1994.

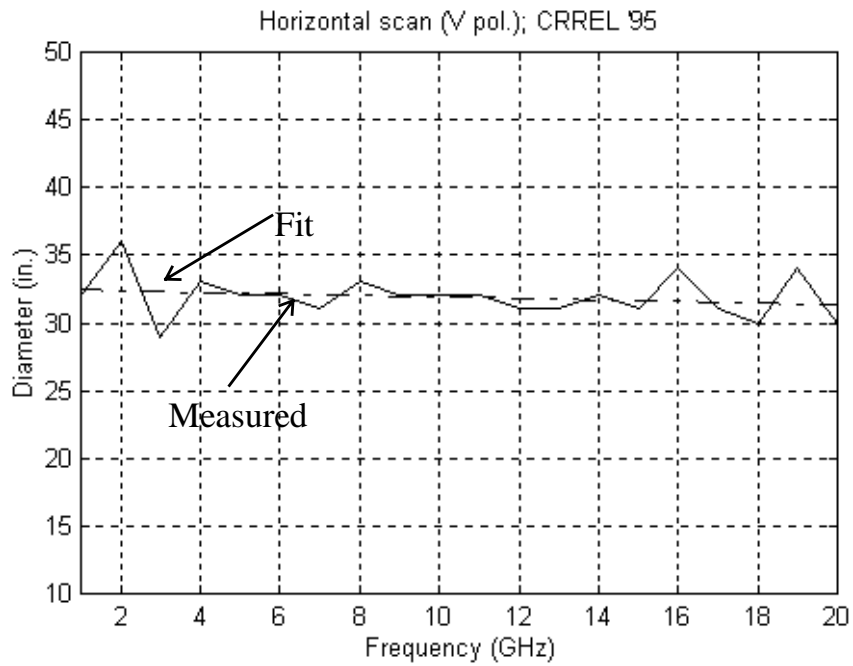


**Figure 4.1(c)** Horizontal distance used for illuminated area calculation in 1995.

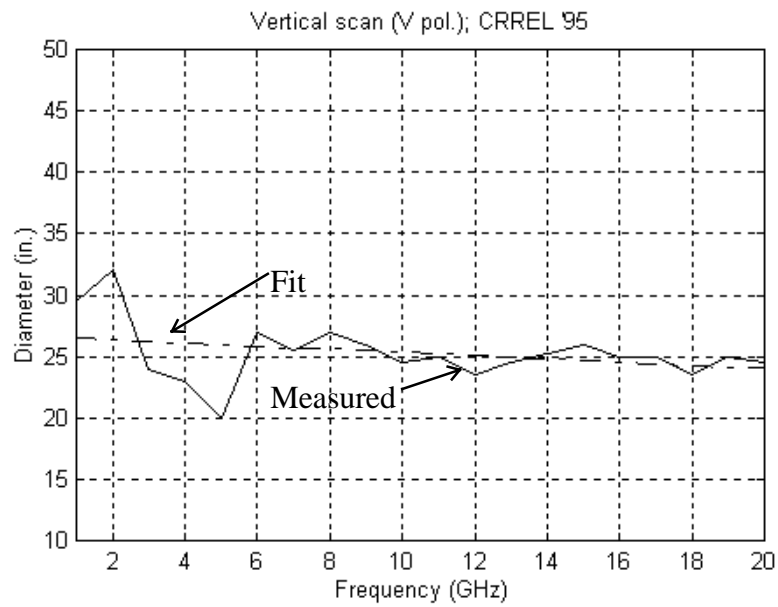


**Figure 4.1(d)** Vertical distance used for illuminated area calculation in 1995.

To extract the scattering coefficient of the ice, we need first to determine the return power as a function of frequency. The chart in figure 4.2 below illustrates the steps involved in extracting the frequency response of the return from ice,  $P_r(f)$ .

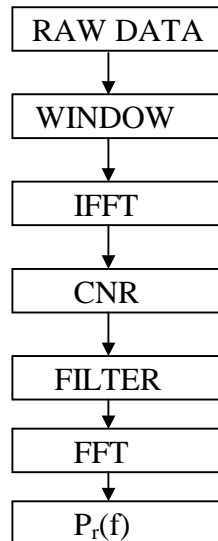


**Figure 4.2** Data processing steps to extract frequency response of return from ice.

## 4.2 Signal Processing

### Windowing and Zero Padding

Window is applied on the raw frequency-domain data (figure 4.3) to minimize the effect of spectral leakage (range sidelobes). We chose the Hamming window, which maintains a reasonably sharp central peak with a 40-dB reduction in the first sidelobe. The windowed data (figure 4.4) are then padded with zeros the size of the data, as in circular convolution, to prevent the large signal from one end dominating a smaller signal at the other end during the filtering process.

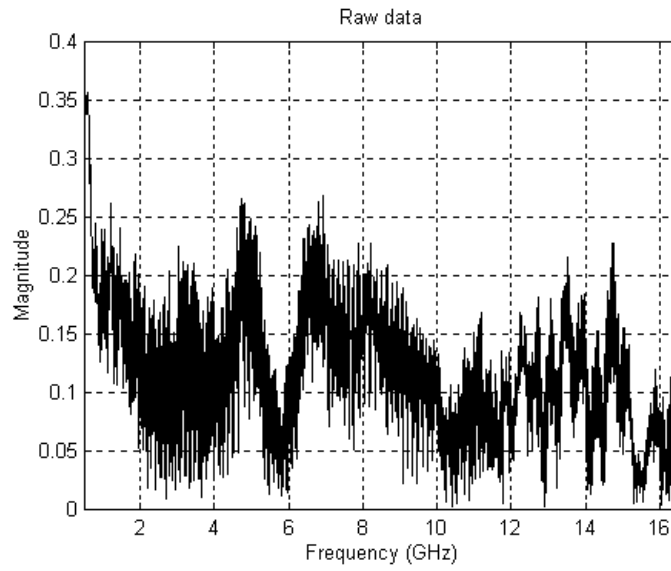


**Figure 4.3** Raw step-frequency radar data.

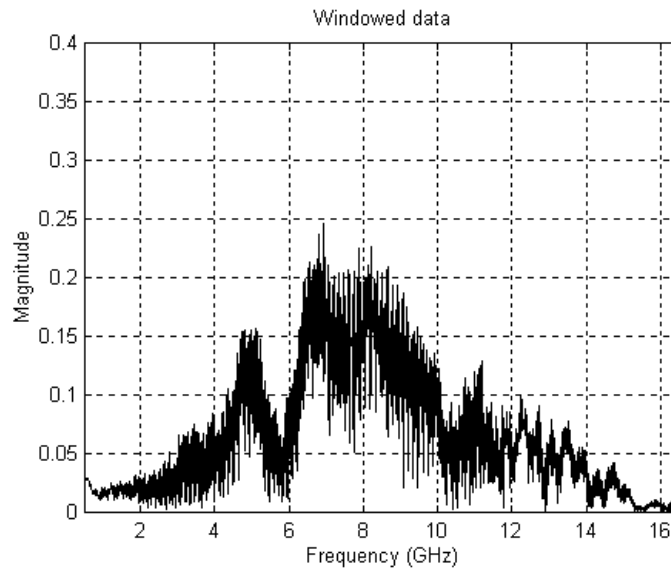


**Figure 4.4** Windowed data.

### IFFT & Coherent Noise Reduction (CNR)

Since the data were collected in a single antenna mode, we know from (2.8) that the IFFT of the signal will give a spectrum of all the scatterers, which includes that of

the reflection from the antenna and feedthrough (figure 4.5). These signals are usually much stronger than those of the target, especially at higher incidence angles ( $>10^\circ$ ). At these angles, the return from the ice is barely visible.

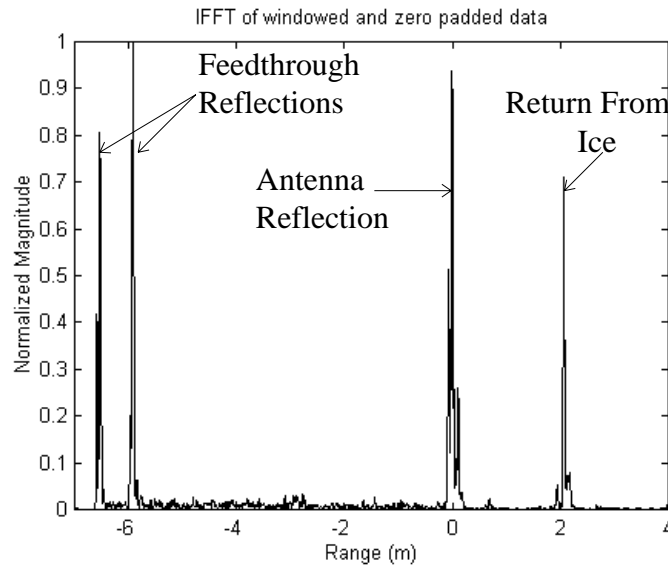


**Figure 4.5** Impulse response of windowed and zero-padded data.

Usually, there are two ways that these unwanted reflections are reduced. The first way is to subtract coherently the background return from that of the ice. This can be accomplished by pointing the antenna to the sky, but we could not do this because of the limited extension range of the actuator. The second way is to implement a hardware range gate to suppress these unwanted reflections, but this technique requires very fast switches for short ranges. We tried range gating with a commercial hardware range gate, the LINTEK Range Gate, but we were unsuccessful using this hardware. To reduce the feedthrough signals we employed the coherent noise reduction (CNR) technique [Beaven, 1995]. The primary assumption of this technique is that the phase of the return

from a distributed target varies randomly from one sample to another while the phase of the feedthrough signals remains constant. CNR is carried out by coherently averaging several independent samples at each angle and subtracting the average from each sample. Coherent averaging reduces the return from the target because of the varying phase and gives us an estimate of the system noise, which is coherent. If we have  $N$  independent samples ( $V_1 \dots V_N$ ), CNR applied to  $V_1$  is simply

$$V_{1CNR} = V_1 - \frac{1}{N} \sum_{i=1}^N V_i \quad (4.3)$$

Figure 4.6 shows an example of CNR done on  $15^\circ$  return from pancake ice.

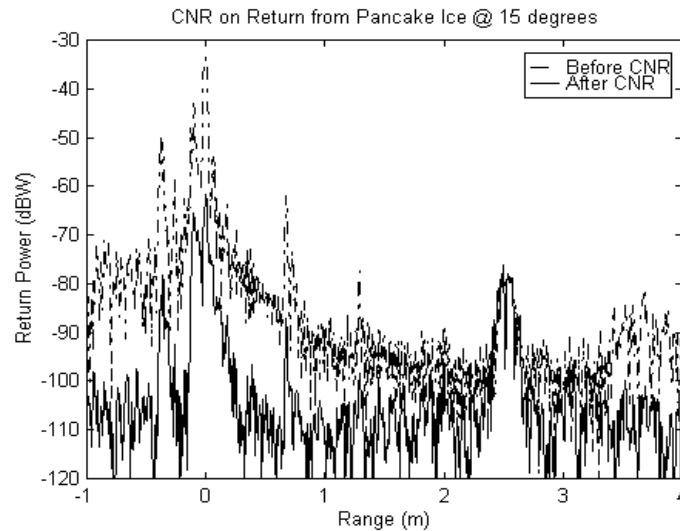


**Figure 4.6** Result of CNR on pancake ice at  $15^\circ$  incidence angle. These data were collected using the plane-wave system during the CRRELEX '95 experiment.

## Filtering & FFT

To isolate the ice return from other signals in the range domain (figure 4.7), we need to design a narrowband bandpass digital filter. We used a Gaussian filter in the range domain to reduce the ringing in the frequency domain. The ringing effect of a rectangular filter on simulated data is shown in figure 4.8. Notice the reduction in ringing when a Gaussian filter is used in figure 4.9(a).

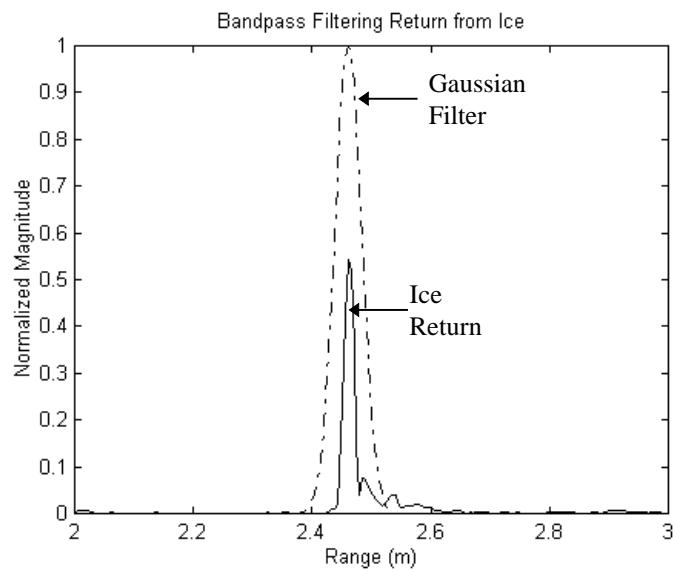


**Figure 4.7** Isolating return from ice.

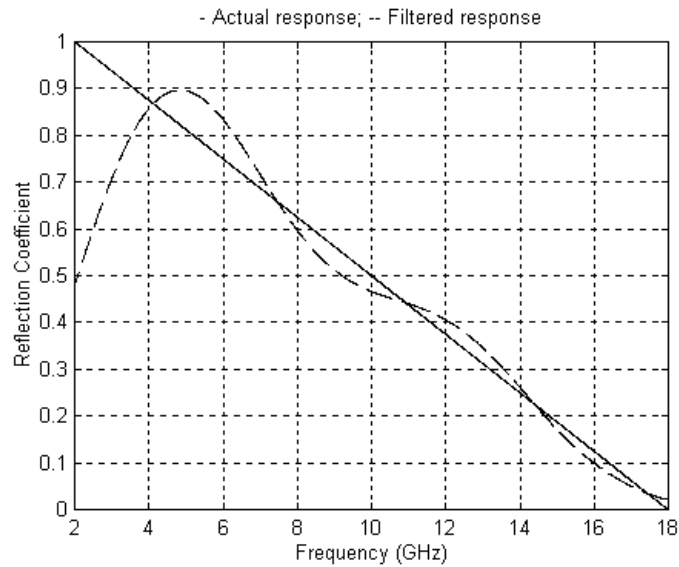


**Figure 4.8** Frequency response of data filtered with a rectangular filter.

The following is the filtering sequence used to extract the wideband response of the return.

- 1) From the IFFT of the signal determine the return associated with the target and synthesize a Gaussian bandpass filter centered on the return from the ice.
- 2) FFT of the filtered signal will give us the frequency response of the ice return. The drawback to this response is the effect of the filter's transient response (figure 4.8(a)) to the range-domain band edge, where the transfer-function response is assumed to go abruptly to zero.
- 3) To reduce the ringing effect, we created a correction factor for the frequency response [Higgins, 1990]. This is done by simulating the step-frequency data (2.4(c)) with a reflection coefficient of one with the range being set equal to that of the target. The same process of windowing, zero padding and IFFT performed on the measured data is

repeated for the simulated data. The filter used for the simulated data should be identical to that of the target. The FFT of this filtered signal is the correction factor that is divided by the frequency response of the target. Figure 4.9 (a) and (b) shows the effects of filtering simulated data with and without the correction factor. The filter's passband passed only 4 range cells ( $4 \cdot \Delta R$ ). The corrected frequency response has about 5% error at the edges. Notice the ringing effect in the beginning of the uncorrected filtered response.

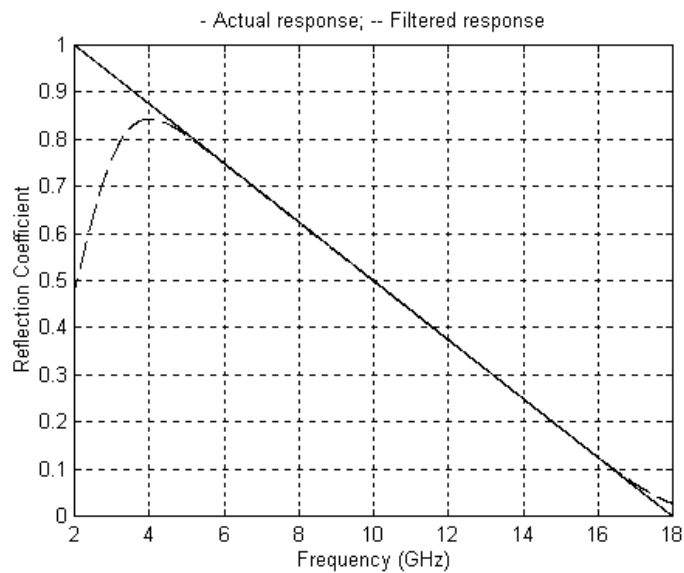


**Figure 4.9(a)** Frequency response of filtered data using Gaussian filter.

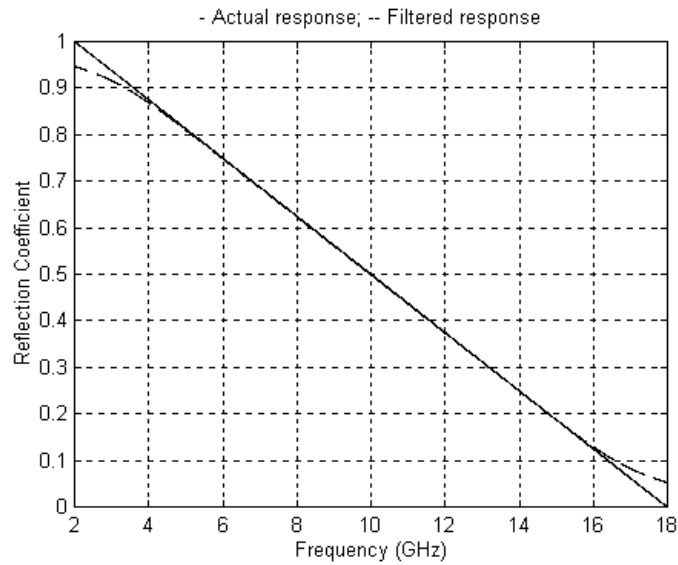


**Figure 4.9(b)** Frequency response of data filtered with a Gaussian filter with correction factor applied.

The effectiveness of the correction is dependent on the width of the filter passband. The larger the filter passband, the more accurate will be our frequency response, but widening the filter may include spurious responses from our measured data. For low incidence angles ( $0^\circ$ - $10^\circ$ ), two to four range cells in the passband are sufficient to obtain the frequency response. For higher incidence angles a wider passband may be used. The corrected frequency response of the target,  $P_r(f)$ , is used in (4.1) to compute the backscattering coefficient. Figure 4.10 shows an example of the frequency response,  $P_r(f)$ , of the return from pancake ice at  $0^\circ$ .

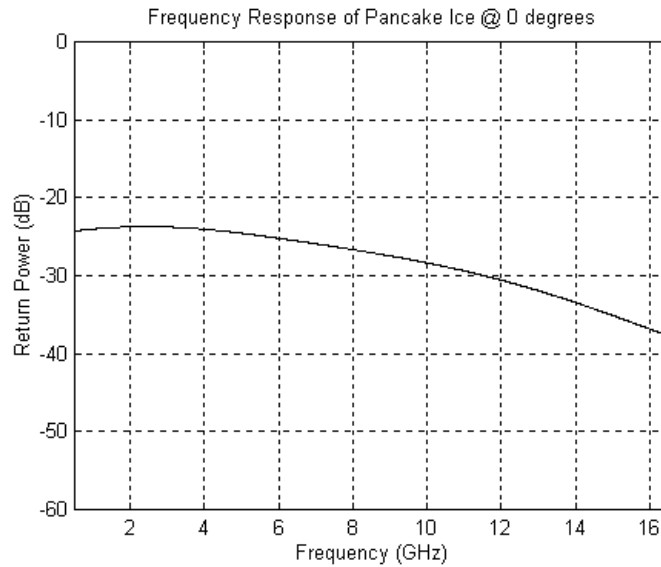


**Figure 4.10** Uncalibrated return power as a function of frequency for pancake ice at  $0^\circ$ .

### 4.3 Calibration

Our measurements were calibrated using an 8-inch-diameter metal sphere. The theoretical scattering response for the metal sphere in figure 4.11 shows that the scattering is in the Mie region below 5 GHz. To recover accurately the response of the sphere from the measured result, we need to recover the main return and the amplitude modulated components shown in figure 4.12. The amplitude-modulated components are due to the sinusoidal nature of scattering in the Mie region. From figure 4.13 the measured impulse response of sphere, we cannot see these amplitude-modulated components. These components could be buried in noise, since the signal-to-noise ratio of these components is only about 15 dB theoretically under ideal conditions (i.e., no sensitivity limitations, no noise, etc.). Due to this error in calibration, our data are only valid from 5 GHz onward.

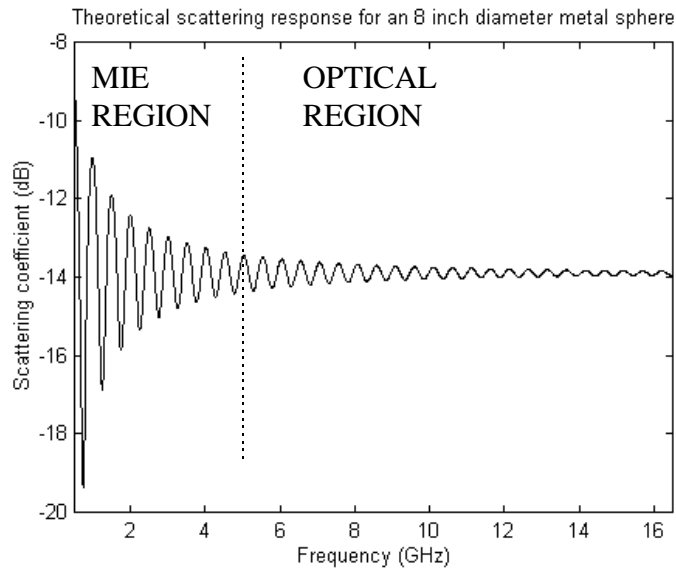


**Figure 4.11** Theoretical scattering response of an 8-inch-diameter sphere.

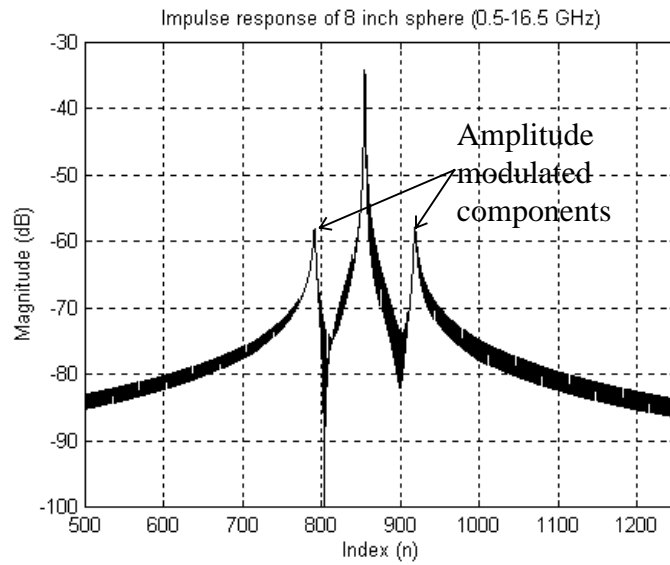


**Figure 4.12** Ideal impulse response for an 8-inch metal sphere.

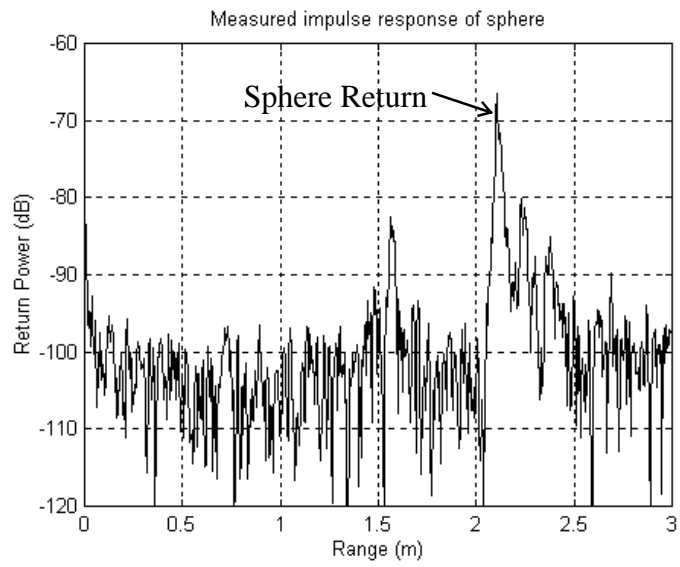


**Figure 4.13** Measured impulse response of sphere.

## Chapter 5

### Scattering Theory

A brief review on scattering theory related to sea ice is given to provide some background on the scattering mechanisms of sea ice.

When an electromagnetic wave illuminates the boundary layer between two mediums of differing permittivity, a portion of this wave's energy is reflected and the rest is transmitted into the second medium. When the second medium is homogeneous, we will find surface scattering. When the second medium consists of materials of varying permittivities, the scattering from these materials is referred to as volume scattering.

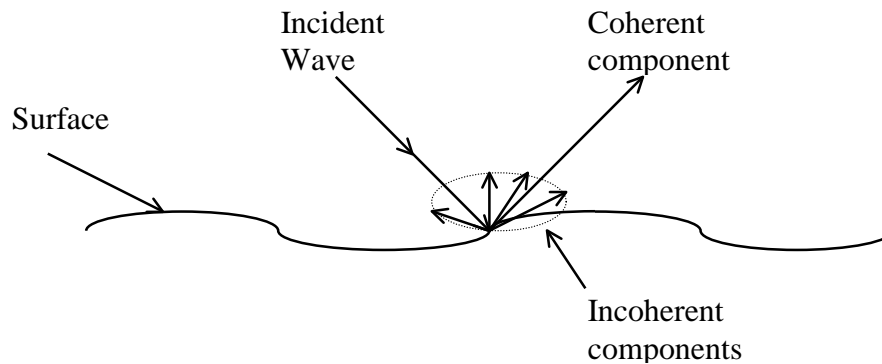


**Figure 5.1(a)** Typical surface scattering pattern.

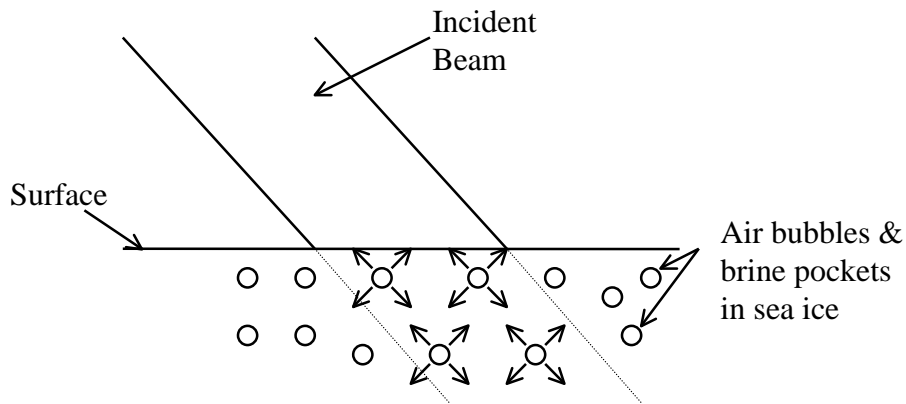


**Figure 5.1(b)** Typical volume scattering pattern.

The reflection of an electromagnetic wave from a smooth surface is called the specular or coherent component and the direction of reflection is called the specular direction. Figure 5.1(a) shows the typical nature of surface scatterer. As the roughness of the surface increases, the reflection in the specular direction begins to decrease as the incident wave's energy is redistributed in several other directions. These scattered components are called the incoherent components. Theoretically, a monostatic radar should not be able to receive the return power from a smooth surface at incidence angles other than nadir. The primary component seen at incidence angles greater than zero is the incoherent component, whose magnitude is typically larger when the surface is rougher. The roughness of a surface seen by the radar is highly dependent on the wavelength. The smaller the wavelength, the rougher the surface seen by the radar. Volume scattering usually takes place when there is a dielectric discontinuity within the volume. For sea ice, the main contributors of volume scatter are air bubbles and brine pockets. Figure 5.1 (b) shows an example of volume scattering. Figure 5.2 (a) shows a

return from pancake ice at  $0^\circ$ . Notice that there is only a strong surface return at  $0^\circ$ . At  $15^\circ$  (figure 5.2 (b)), there are more returns from the ice; these returns can be the incoherent components from both the surface and volume.

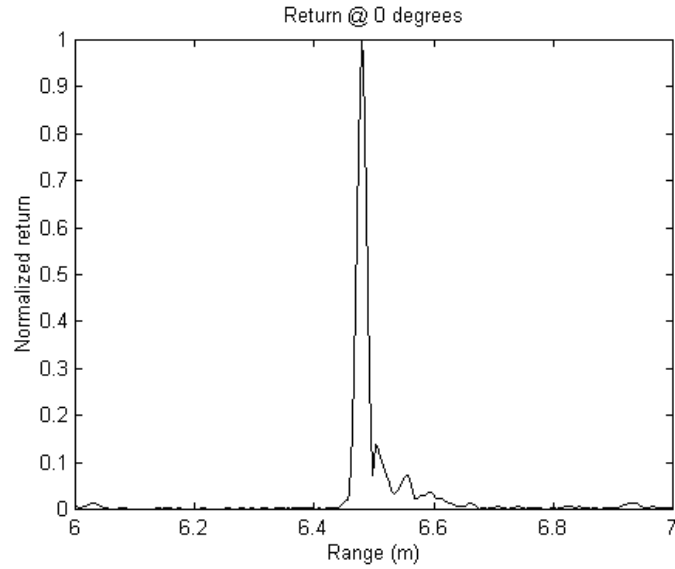


**Figure 5.2 (a)** Example of a primarily coherent return from pancake ice @  $0^\circ$ .

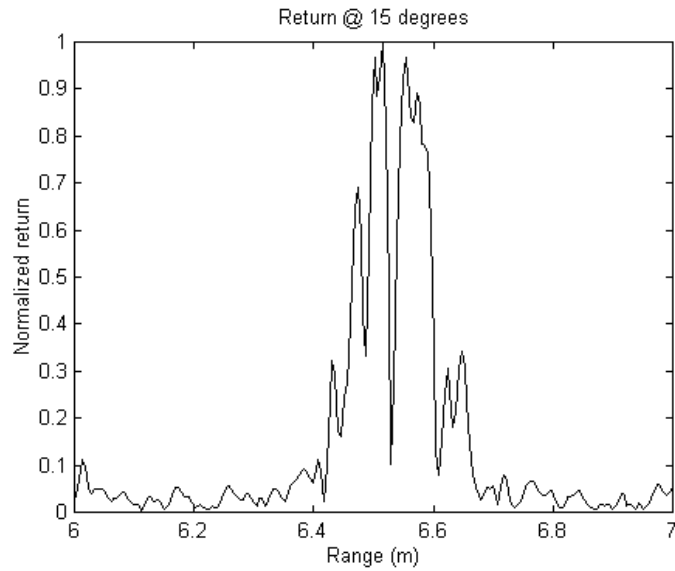


**Figure 5.2 (b)** Example of a primarily incoherent return from pancake ice @  $15^\circ$ .

A more detailed discussion on determining the contribution from coherent and incoherent components from sea ice and the parameters that influence scattering from sea ice can be found in Beaven [1992] , Gogineni [1984] and Kim [1984].

## Chapter 6

### CRRELEX Results

The results of the CRREL experiments are presented in three parts in this chapter. The first part consists of a few impulse response plots of the various ice types, namely, bare ice and snow-covered ice at a few angles (the impulse responses of pancake ice have been shown in figures 5.2(a) and (b)). The second part consists of angular responses of the scattering coefficients for the above-mentioned ice types at C band and Ku band. A comparison between the scattering coefficients obtained using the plane-wave and the spherical-wave antenna is shown here. Comparison with field measurements for pancake ice is also made in this section. The third part consists of frequency responses of the scattering coefficients at various incidence angles.

#### 6.1 Impulse Response

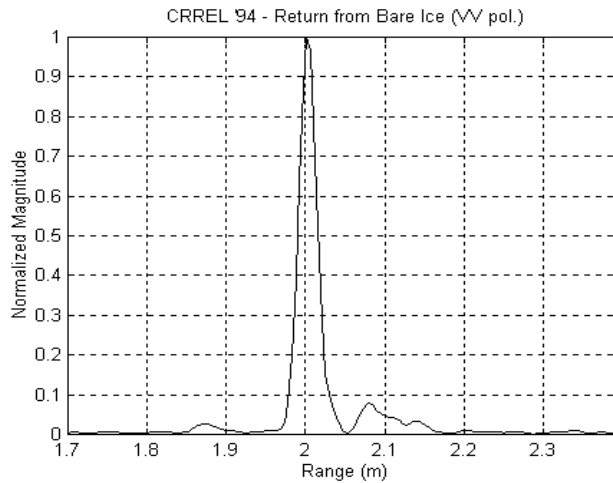


**Figure 6.1** Return from bare ice at  $0^\circ$ .

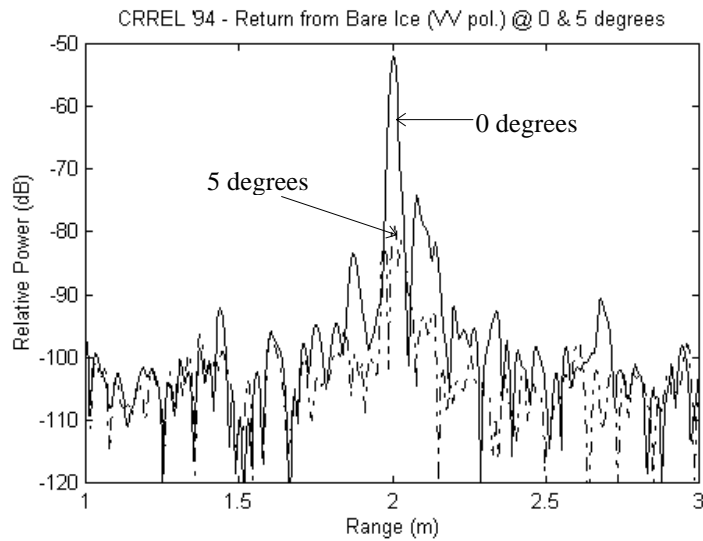


**Figure 6.2** Return from bare ice at  $0^\circ$  and  $5^\circ$ .

Figure 6.1 shows the typical response from bare ice at nadir. The return from smooth bare ice resembles a delta function at nadir. As the incidence angle is increased to  $5^\circ$ , the return power drops by almost 30 dB (figure 6.2). This demonstrates the excellent angular resolution that we are able to achieve with our system.

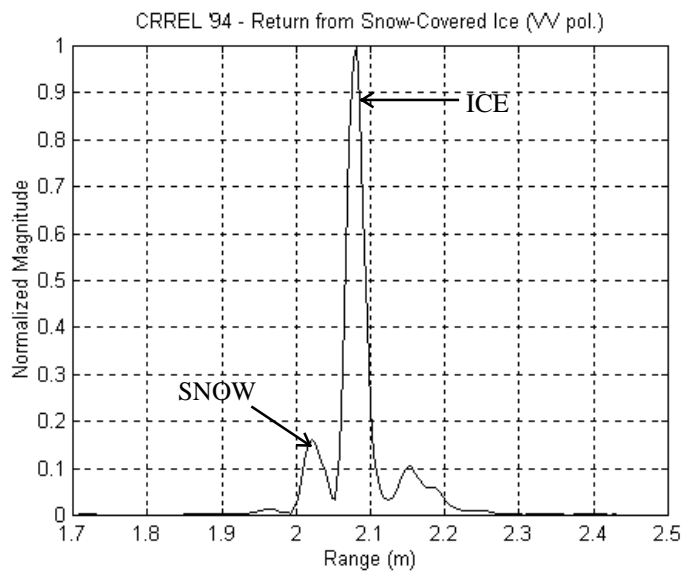


**Figure 6.3** Return from snow-covered ice at  $0^\circ$ .

Figure 6.3 demonstrates the excellent resolving capability of the plane-wave system. Notice the clear reflections from the air/snow and the snow/ice interfaces, which are about 5 cm apart. The reflection from the snow/ice interface is about seven times higher than that from the air/snow interface. This is due to the higher dielectric constant of the ice. We used a resonant probe to measure the dielectric constant of ice and snow. The resonant frequency of the probe was measured in free space and the medium. The relationship between the resonant frequency of the probe in the medium and its dielectric constant is given by

$$\frac{\epsilon_{med}}{\epsilon_{air}} = \left( \frac{f_{air}}{f_{med}} \right)^2 \quad (6.1)$$

where  $\epsilon_{med}$  &  $\epsilon_{air}$  are the dielectric constants of the medium and air, respectively, and  $f_{med}$  &  $f_{air}$  are the resonant frequencies of the probe in the medium and air, respectively.

The dielectric constants of ice and snow were measured to be 3.5 and 1.17, respectively. The relationship between the reflection coefficient and the dielectric constant of a material is given by

$$\Gamma = \frac{\sqrt{\epsilon_2/\epsilon_1} - 1}{\sqrt{\epsilon_2/\epsilon_1} + 1} \quad (6.2)$$

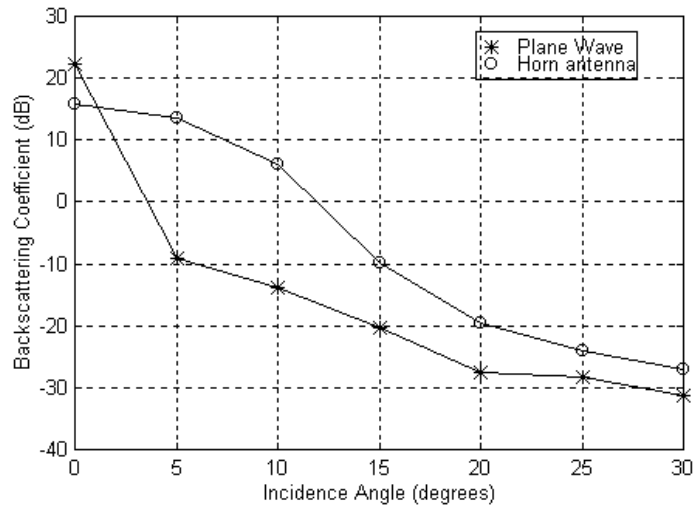
where  $\Gamma$  is the reflection coefficient at the dielectric interface and  $\epsilon_1$  &  $\epsilon_2$  are the dielectric constant of medium 1 and medium 2, respectively.

The reflection coefficients at the snow/ice interface and air/snow interface were found to be 0.266 and 0.0406, respectively. The ratio of the reflection coefficient from the ice to snow is 6.56:1. This agrees with our measured result shown in figure 6.3.

## **6.2 Angular Scattering Response**

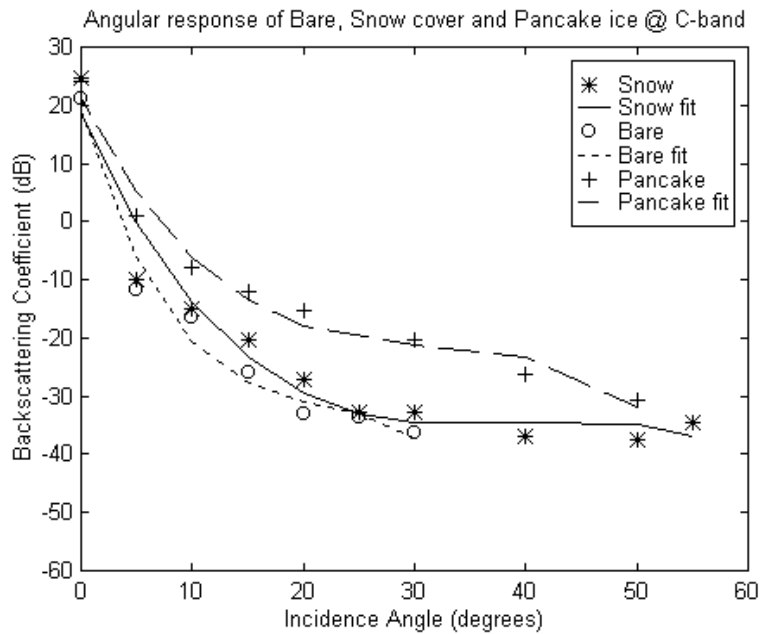
The scattering responses were computed and calibrated to a metal sphere with a radar cross section,  $\sigma_{\text{cal}}$ , of -13.9 dB as in (4.1).

Figure 6.4 illustrates how wide-beam (spherical-wave) antennas corrupt the scattering response from bare ice at near vertical incidence. The scattering coefficient obtained using the plane-wave system at  $5^\circ$  is 25 dB lower than that obtained using the conventional system. The results of the wide-beam antenna are corrupted by scattering from vertical until the incidence angle increases to about  $20^\circ$ . This result confirms the superiority of the plane-wave system over conventional systems for measuring the scattering response for vertical incidence. The 3- to 4-dB difference in scattering at angles greater than  $20^\circ$  could be due to the difference in roughness characteristics of the two surfaces.



**Figure 6.4** Comparison of backscattering coefficient from bare ice obtained using plane-wave and spherical-wave antennas at Ku band.

Figures 6.5 and 6.6 below show the angular response of several ice types at C band and Ku band respectively. From the plots above we can see that the scattering for pancake ice is higher than bare ice for angles greater than zero. The results show that there is more incoherent scattering from pancake ice because of its rougher surface. The scattering from snow-covered ice is slightly higher than that from bare ice because of the slightly rougher surface. We can also see for the three ice types that surface scattering may dominate, at least until 30°, because of the scattering coefficient fall off with angle.



**Figure 6.5** Angular response of bare ice, snow-covered ice and pancake ice at C band.

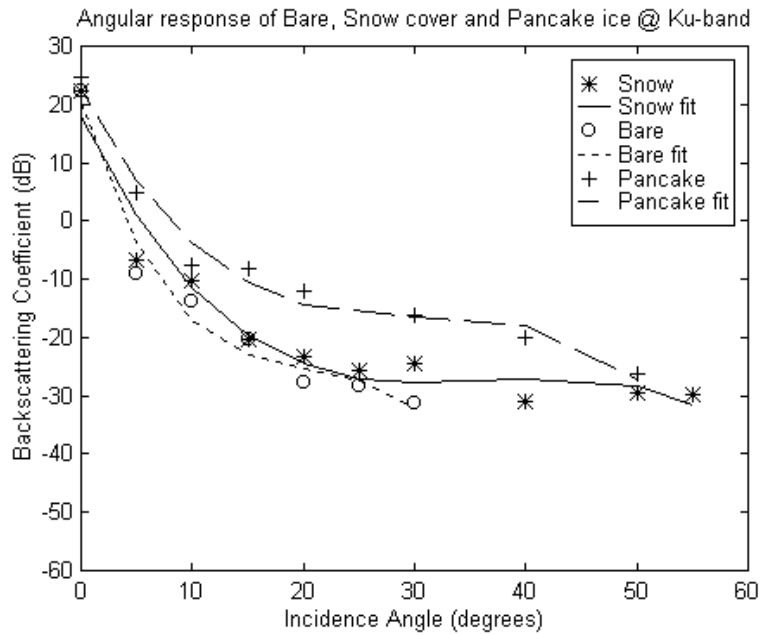


**Figure 6.6** Angular response of bare ice, snow-covered ice and pancake ice at Ku band.

Backscatter from pancake ice is influenced by “the roughness of the upturned edges of the cake, the degree of compactness of the ice pans, and the degree of wave washing of the individual ice pans.” [Drinkwater et al.,1995]

The backscatter from pancake ice has been known to vary over a wide range (10-20 dB) for a given incidence angle depending on the factors mentioned above [Drinkwater et al.,1995]. Figure 6.7 shows the agreement between field and laboratory backscatter characteristics of pancake ice at 35°. The lower scattering from the laboratory measurement of the pancake ice is mainly due to the less vigorous wave action that caused the formation of elongated pancake ice, which is generally smoother.

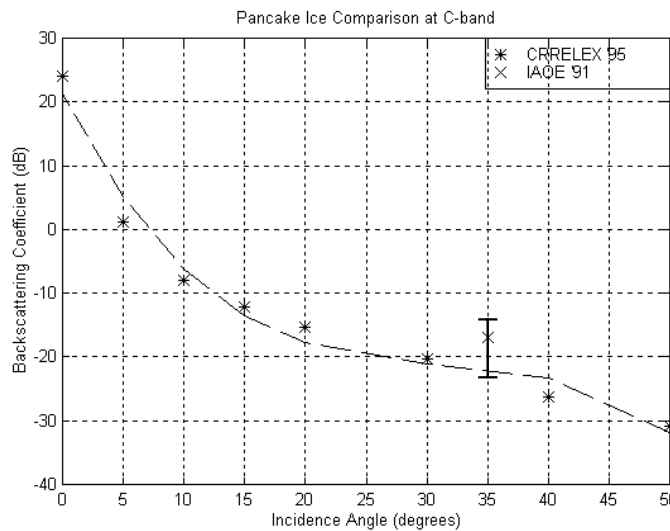


**Figure 6.7** Comparison between field and laboratory measurement of pancake ice.

### 6.3 Frequency Scattering Response

The scattering results shown in this section are only valid from 5 GHz onward because of the calibration error mentioned in Section 4.3.

At  $0^\circ$  (figure 6.8), we see that scattering from pancake ice is increasing with frequency. This shows that at the higher frequencies scattering is dominated by the incoherent term. As for the snow-covered ice, it can be observed that from 5 GHz onward the scattering is decreasing with frequency, which means that the coherent component is decreasing with frequency. As for the bare ice, there is no significant change in the scattering level, which means that there is only a dominant coherent component. To explain the relative scattering levels of these three ice types, more modeling effort is required to determine the contribution from the incoherent and coherent components. When the incidence angle is increased to  $5^\circ$  (figure 6.9), there is a 15- to 20-dB drop in the scattering coefficient of pancake ice and about a 25- to 30-dB drop in the scattering coefficient of bare ice and snow-covered ice. The large drop in the scattering level is due to the reduction in coherent scattering. The scattering for all three ice types increased as a function of frequency. This is an indication of dominant incoherent scattering. The same trend is also observed at  $20^\circ$  (figure 6.10).

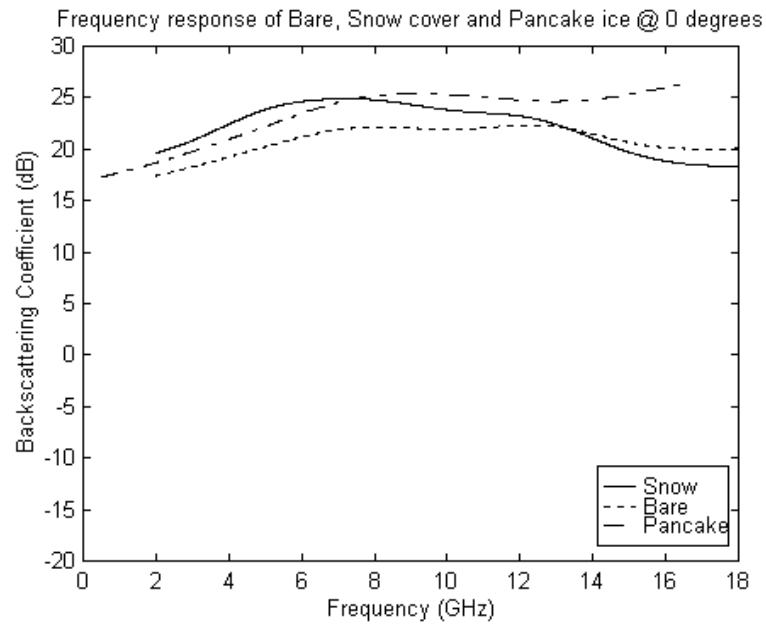


**Figure 6.8** Frequency response of bare ice, snow-covered ice and pancake ice at 0°.

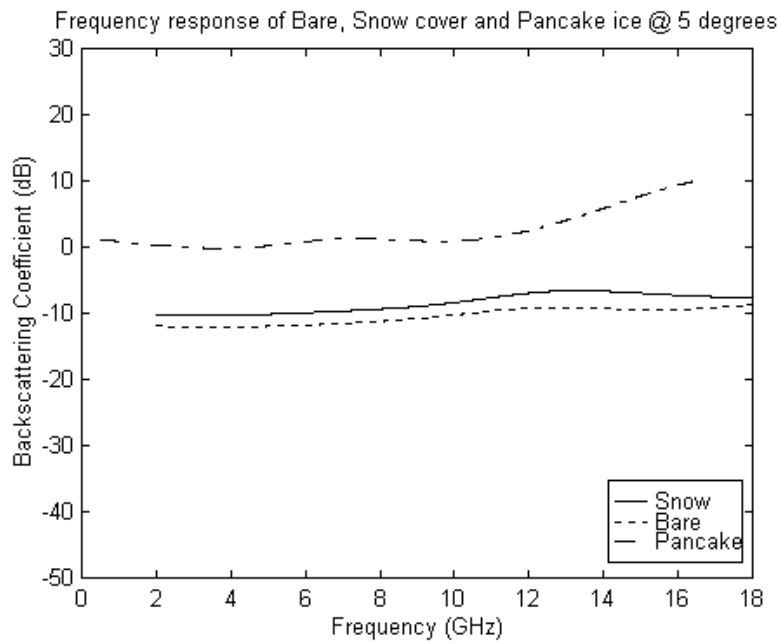


**Figure 6.9** Frequency response of bare ice, snow-covered ice and pancake ice at 5°.

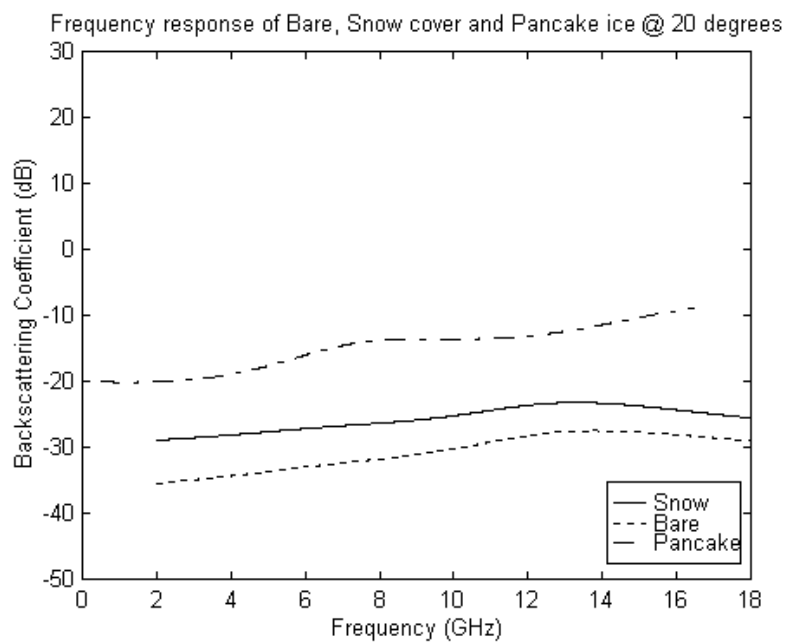


**Figure 6.10** Frequency response of bare ice, snow-covered ice and pancake ice at 20°.

## Chapter 7

### Conclusions and Future Work

An ultra-wideband radar and a plane-wave antenna have been used to measure the high-resolution scattering response of bare saline ice, snow-covered ice and pancake ice during the winter season at the US Army Cold Regions Research and Engineering Laboratory (CRREL) during the 1994 and 1995 winter seasons. We have developed signal processing techniques to extract the wideband response of a signal using narrowband filters in the spectral domain. We have shown how the ringing effect associated with narrowband filters can be reduced by using a correction factor. The results of our measurements show the excellent spatial and angular resolution that can be achieved with the plane-wave system. The scattering coefficients obtained using the plane-wave system show that surface scattering dominates at least until  $30^\circ$ . At  $0^\circ$ , the scattering from bare ice stayed fairly constant with about 1- to 2-dB variation across the 5- to 18-GHz frequency range, while the scattering from pancake ice increased from 16 to 27 dB with increasing frequency. On the other hand, the scattering from snow-covered ice decreased from 24 to 15 dB with increasing frequency. This shows that there is more contribution from incoherent components for pancake ice at higher frequencies, while for snow-covered ice there is less contribution from the coherent component at the higher frequencies. At incidence angles other than  $0^\circ$ , the scattering increased as a function of frequency, which is an indication of dominant incoherent scattering. With increasing incidence angle, the scattering level dropped. This is an

indication of dominant surface scattering. Field measurement of pancake ice at  $35^\circ$  shows agreement with laboratory measurement at the lower bound.

Cepstrum techniques can be employed to determine accurate impulse response of the target by removing system effects such as multiple reflections from mismatches at the network analyzer test port and the antenna feed.

The drooping effect caused by using the narrowband filter can be further reduced by using the Extended Frequency Domain-Prony's Method (EFDPM). The EFDPM technique is used to model the frequency response of a target. In this scheme the coefficients of the numerator and denominator of a rational function are estimated by solving a linear system of equations. These coefficients are then used to model the frequency domain response of a target [Chakrabarti, 1995].

**PART II**

**RANGE-GATED STEP-FREQUENCY RADAR**

**USING THE FM-CW CONCEPT**

## **Chapter 8**

### **Range-Gated Step-Frequency Radar**

#### **8.1 Introduction**

The step-frequency radar has been used extensively in short-range radar measurements to study the scattering properties of geophysical surfaces because of the ease with which it can be implemented and its high-range resolution. The main limitations of the step-frequency radar are its limited unambiguous range and the difficulty in implementing range gating for short ranges. The range of the step-frequency radar is limited by the number of its frequency steps. When the step-frequency radar is operated monostatically, the return is corrupted by reflections from the antenna feed, thus affecting the sensitivity of the system. Currently, range-gating for the step-frequency radar is implemented with very fast switches on the transmit and receive sides to gate out the undesired reflections. Switching times must be on the order of nanoseconds, and the implementation of such switches is difficult.

Some of the problems associated with the step-frequency radar can be overcome by using the frequency-modulated, continuous-wave (FM-CW) radar system. The unambiguous range of the FM-CW radar is usually larger than that of the step-frequency radar. The range gating is easily implemented on the FM-CW radar simply by putting a high-pass filter between the output of the mixer and the IF amplifier. The cut-off frequency of this high-pass filter is chosen to eliminate the reflection from the antenna.

To overcome the problems associated with these two systems, a new system is proposed. The new system combines the range-gating capability of the FM-CW radar and the operation method of the step-frequency radar to obtain a high-resolution range-gated spectrum. The system will also have the ranging capability of the FM-CW radar.

## **8.2 Principles of Operation**

The proposed system measures the amplitude and phase of the range-gated FM signal at each of the frequency steps. The amplitude and phase at each of these frequencies are identical to the step-frequency radar data. To understand the operation of this system we must first understand the operation of the FM-CW radar and the step-frequency radar (refer to Chapter 2 for step-frequency radar operation).

### *8.2.1 Principles of FM-CW Radar Operation*

The FM-CW radar frequency modulates a signal over some bandwidth. The bandwidth of this signal determines the range resolution. The larger the bandwidth, the higher the range resolution. The return signal from the target is then compared to the transmitted wave to extract the range, amplitude and phase information of the target. The difference between the return signal and the transmitted signal is known as the IF or beat signal. Figure 8.1 shows a typical transmit and receive waveform from a point target.

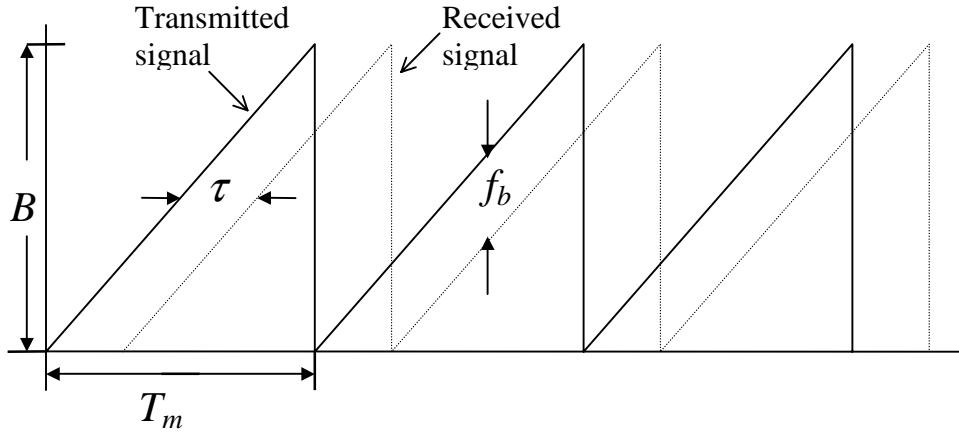


**Figure 8.1** Transmit and receive signal from a point target for an FM-CW radar.

The time it takes for the signal to travel the two-way distance between the target and the radar is  $\tau$ . Hence,

$$\tau = \frac{2R}{c} \quad (8.1)$$

From the geometry of the transmit and receive waveforms we can derive a relationship between the beat frequency ( $f_b$ ) and the range ( $R$ ). The beat frequency is the instantaneous difference frequency between the transmitted and received signal.

For the sawtooth modulation we can see that

$$\frac{\tau}{T_m} = \frac{f_b}{B} \quad (8.2)$$

Substituting (8.1) into (8.2) and rearranging the equation, we have

$$f_b = \frac{2RBf_m}{c} \quad (8.3)$$

where  $R$  is the range to the target,  $B$  is the FM sweep bandwidth,  $f_m$  is the modulation frequency of the sawtooth waveform,  $c$  is the speed of light and  $f_b$  is the beat frequency.

For multiple targets the beat signal will consist of several frequencies. The Fourier transform of the beat signal will give us the spectral components of each of these targets. The minimum two-way travel time,  $\tau_{\min}$ , for the signal is

$$\tau_{\min} = \frac{1}{B} \quad (8.4)$$

Substituting (8.4) into (8.1) we can see that the range resolution ( $\Delta R$ ) for the FM radar is

$$\Delta R = \frac{c}{2B} \quad (8.5)$$

From the above equation it can be observed that the range resolution is determined by the sweep bandwidth.

### 8.2.2 Principles of Operation of the Range-Gated Step-Frequency Radar

The transmitted FM signal is given by

$$v_t(t) = A \cos(2\pi f_c t + \pi B f_m t^2 + \theta_o) \quad (8.6)$$

where  $f_c$  is the center frequency.

The received signal at the mixer output is given by

$$v_r(t) = \sum_i |\Gamma_i| A \cos(2\pi f_{bi} t + 2\pi f_c \tau_i + \pi f_{bi} \tau_i + \phi_i) \quad (8.7)$$

where  $|\Gamma_i|$  is the magnitude of the reflection coefficient of target at location  $i$  and  $\phi_i$  is the phase of  $\Gamma_i$ .

From the above equation it can be observed that at each time,  $t$ , the beat signal,  $v_r(t)$ , contains a summation of the scattering response from all the scatterers. The FFT of the signal,  $v_r(t)$ , will give us the magnitude and phase response of the scatterers at each beat frequency. A high-pass filter with a cutoff frequency slightly higher than that for the antenna placed at the output of the mixer will suppress the antenna reflection.

The FFT of  $v_r(t)$  is given by

$$V_{fft}(f_b) = |\Gamma_{fb}| \exp(j\psi_{fb}) \quad (8.8a)$$

where  $|\Gamma_{fb}|$  is the magnitude of the reflection coefficient of the target corresponding to the beat frequency,  $f_b$

$$\psi_{fb} = 2\pi f_c \tau_{fb} + \phi_{fb} \quad (8.8b)$$

where  $\tau_{fb}$  is the two-way time to the scatterer and back and  $\phi_{fb}$  is the phase of  $\Gamma_{fb}$ .

At the beat frequency corresponding to the target, the spectrum will contain the amplitude and phase information of the target corresponding to the center frequency,  $f_c$ . For each step of the center frequency, the amplitude and phase information of the target is stored. We now have a set of step-frequency radar data that is given by

$$H(i) = |\Gamma_{tar}| \exp\{j(2\pi f_i \tau_{tar} + \phi_{tar})\} \quad (8.9)$$

where  $f_i = f_o + i\Delta f$  and  $\Delta f$  is the frequency step size.

By expanding (8.9) we now have

$$H(i) = |\Gamma_{tar}| \exp\{j(2\pi f_o \tau_{tar} + 2\pi \Delta f \tau_{tar} i + \phi_{tar})\} \quad (8.10)$$

Taking the FFT of  $H(i)$  with respect to  $i$  will give us the high-resolution spectral response of the target. The range to the target can be computed as follows:

The time resolution ( $\Delta t$ ) of the step-frequency radar is given as

$$\Delta t = \frac{1}{N\Delta f} \quad (8.11)$$

where  $N$  is the number of frequency steps taken. Substituting  $\Delta t$  for  $\tau$  and  $\Delta R$  for  $R$  in (8.1) we obtain the relationship between the range resolution and time resolution.

$$\Delta R = \frac{\Delta t \times c}{2} \quad (8.12)$$

The index location of the target is equal to  $\Delta f \tau_{tar}$ , which varies from 0 to N-1 (N is the number of frequency steps). The range (R) to the target can be computed as

$$R = \Delta R \Delta f \tau_{tar} \quad (8.13)$$

The chart below summarizes the steps involved in obtaining the high-resolution range-gated step-frequency spectrum from the FM-CW spectrum.

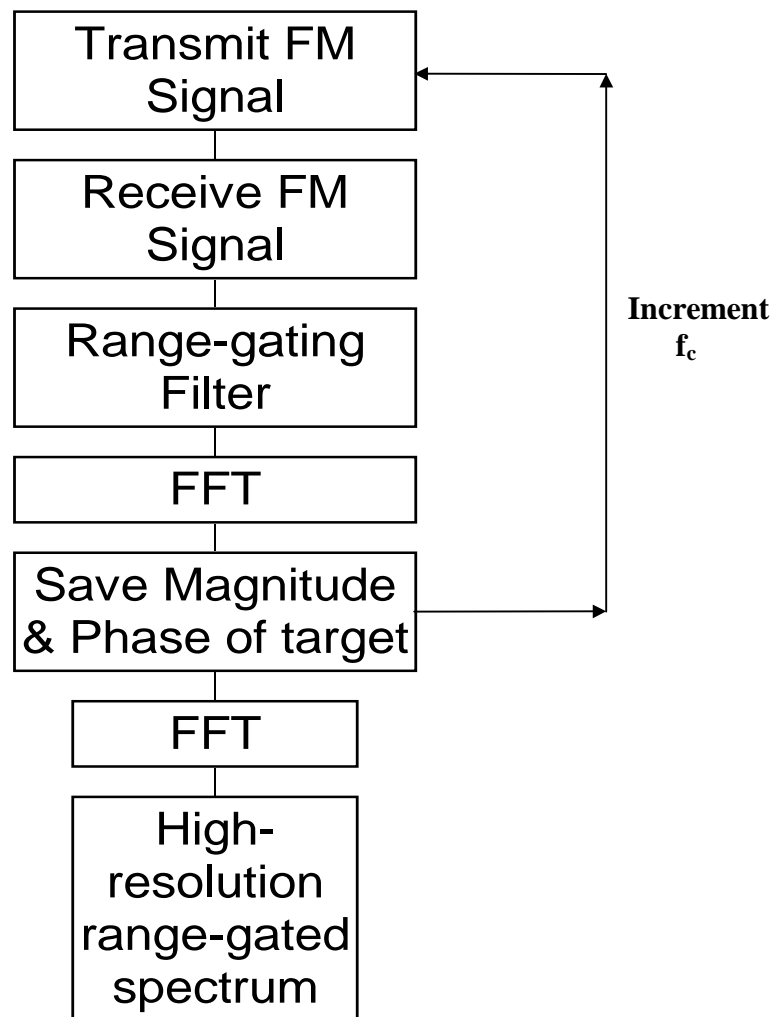


**Figure 8.2** Processing steps for the range-gated step-frequency radar.

### 8.3 Simulation

The range-gated step-frequency radar described in the previous section was simulated using MATLAB to verify the concept. For completeness, several cases have been simulated.

Case 1.

a) Linear sweep from 2 - 18 GHz

b) Single target at 5m.

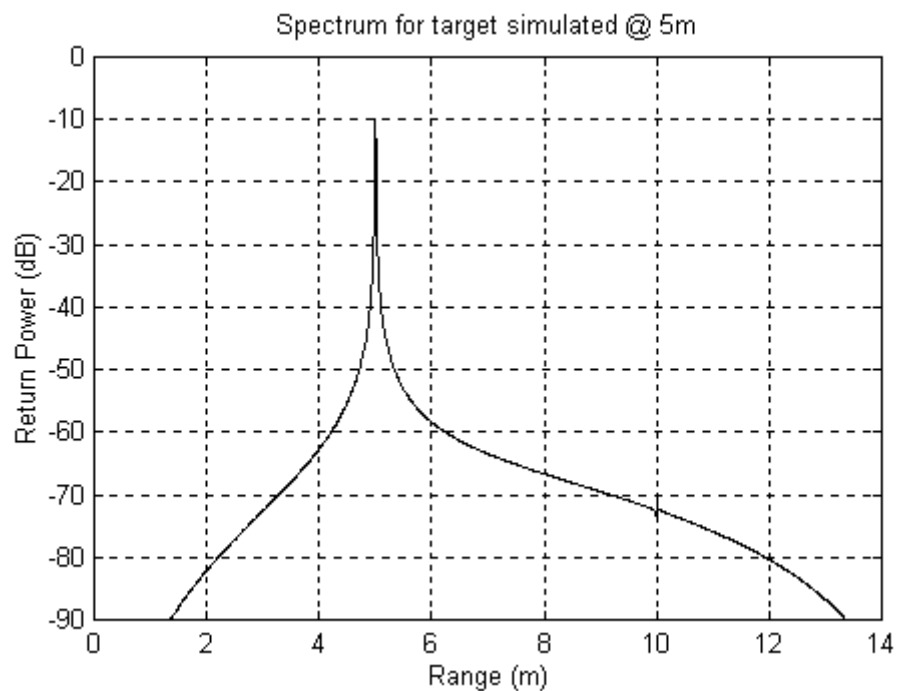


**Figure 8.3** Single target simulated at 5m.

Case 2

a) Linear sweep from 2 - 18 GHz

b) Two targets at 5m and 5.05m, respectively.

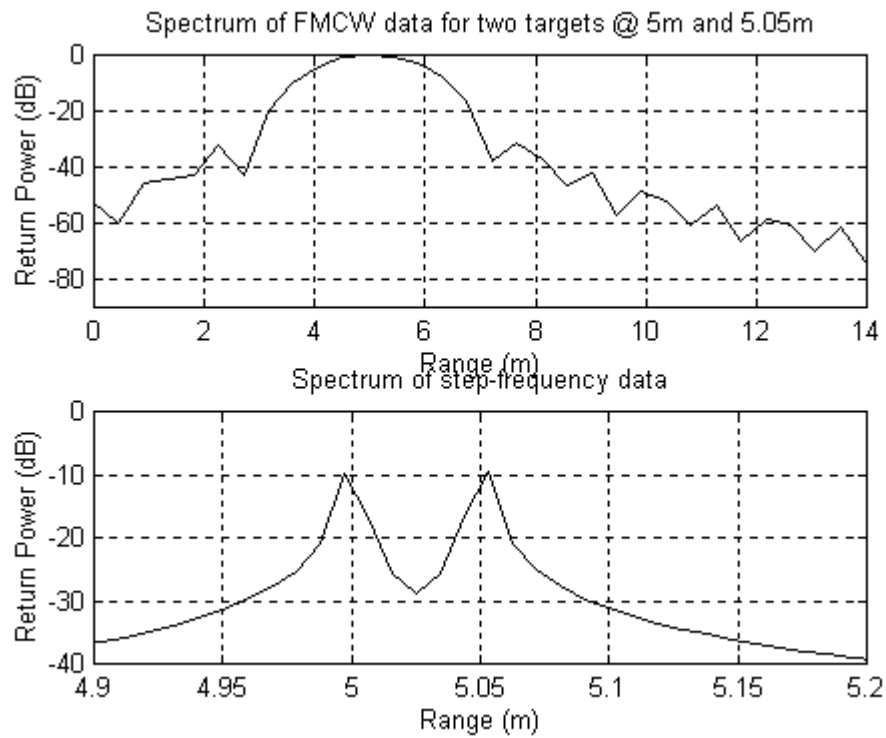
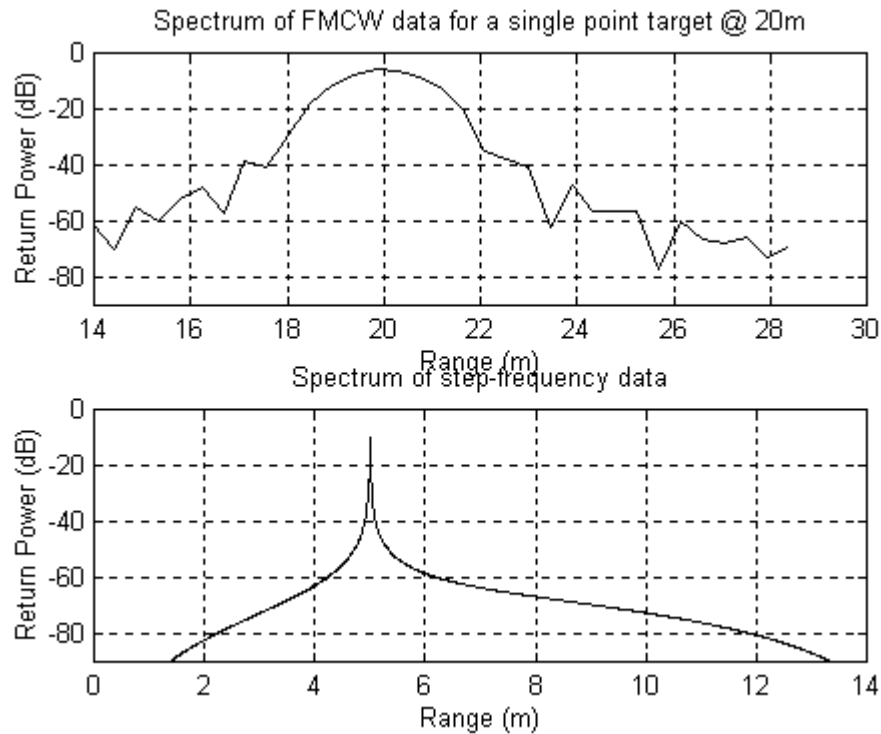


**Figure 8.4** Two targets simulated at 5m and 5.05m, respectively.

Figure 8.4 illustrates the excellent resolving capability of the step-frequency radar when operated in a wideband mode. Notice how it is able resolve the two targets, which are only 5 cm apart.

Case 3

- a) Linear sweep from 2 - 18 GHz
- b) Single target at 20m.



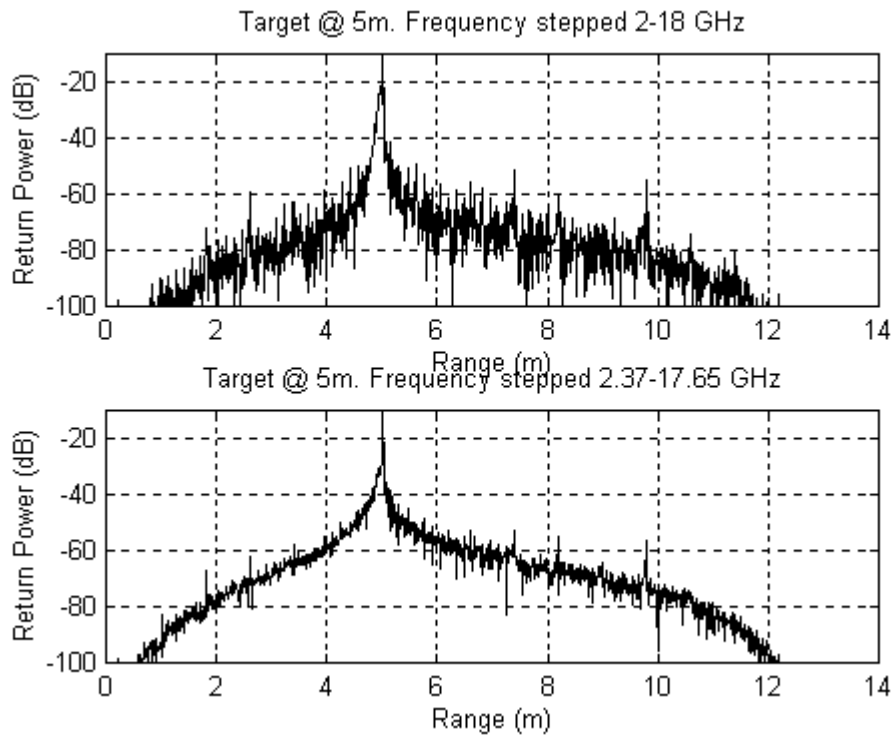
**Figure 8.5** Single target simulated at 20m.

Figure 8.5 illustrates that the step-frequency radar's range is equivalent to the FM radar's range. Previously, by using the network analyzer as a step-frequency radar, we could not see any targets beyond 15m, which is the range limit determined by the number of points and the sweep bandwidth. With this configuration, the spectrum is simply wrapped around and the range can be determined easily from the above plot by adding 15m to the displayed range.

Cases 4 & 5

a) Oscillator's actual frequency sweep from 2 - 18 GHz (case 4) and 2.37 - 17.65 GHz (case 5)

b) Single target at 5 m.



**Figure 8.6** Comparison in system performance when oscillator's frequency is swept the entire frequency span (2-18 GHz) and when it is swept in the linear region of operation (2.37 - 17.65 GHz).

From figure 8.6, we can see the degradation in the performance of the radar when the oscillator's frequency steps are not uniform. The linearity of the sweep was determined by measuring the oscillator's actual frequency and removing the straight-line fit from these frequencies. The results of these measurements are presented in Section 8.4.3.1

## 8.4 System Description

Figure 8.7 shows the block diagram of the range-gated step-frequency.

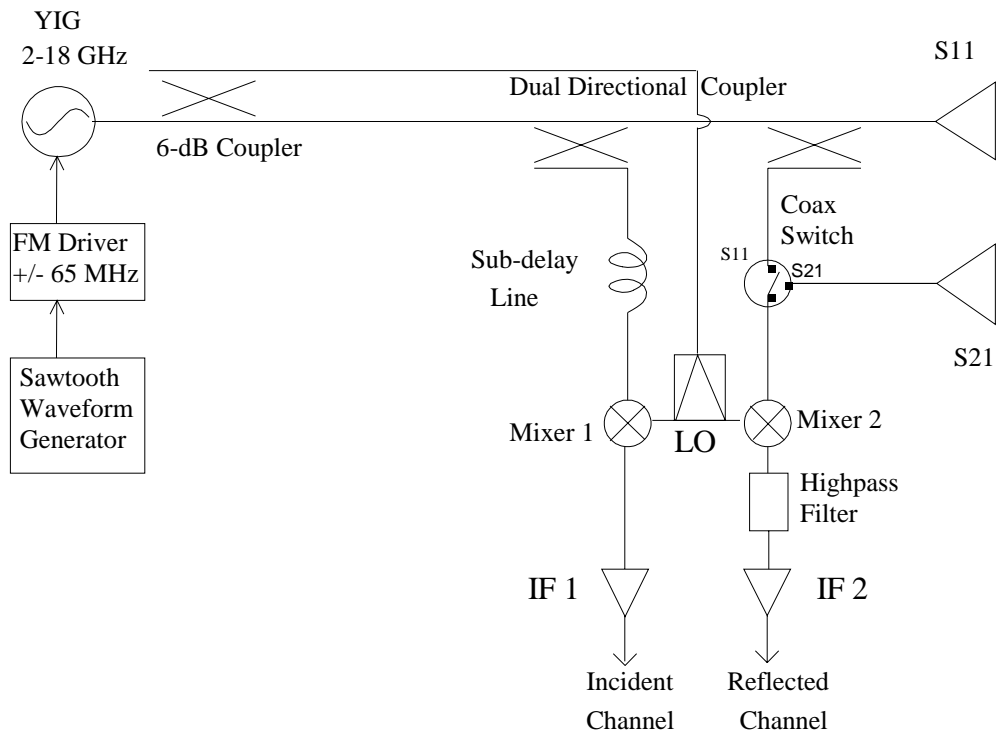


**Figure 8.7** Block Diagram of the Range-Gated Step-Frequency Radar.

The FM-CW radar parameters are summarized in the table below.

**Table 8.1** FM-CW Radar Parameters

<b>Parameter</b>	<b>Value</b>
Center Frequency	2.37 - 17.65 GHz
Center Frequency Step Size	11.7 MHz
Number of Frequency Steps	1300
RF Bandwidth	130 MHz
Range Resolution	1.15 cm
Max. IF Frequency	25 kHz
Sampling Frequency	50 kHz
Max. Unambiguous Range	29 m
Number of Sweeps Averaged	1
Number of Samples per Sweep	50 samples

The selection of the FM-CW radar parameters will be discussed in the following sections. The radar consists of the following modules:

- 1) The waveform generator,
- 2) The FM driver,
- 3) The RF section (YIG Oscillator, 6-dB coupler, dual directional coupler, antenna, coaxial switch, phase trimmer and dual mixer),
- 4) IF Amplifiers,
- 5) Data Acquisition System.

#### 8.4.1 *Sawtooth Waveform Generator*

The sawtooth waveform was generated using the MAX038 evaluation kit. The MAX038 is a high-frequency function generator capable of producing accurate triangle, sine, and square waveforms by changing the appropriate jumper settings. The

sawtooth waveform can be generated simply by changing the duty cycle of the triangular waveform. The factory-assembled evaluation kit generates waveforms from 325 kHz to 10 MHz. The frequency range for the waveform can be set by selecting the appropriate capacitor (C1) from the table given in page 4 of the data sheet [Maxim, 1994]. The frequency of the waveform can then be set by adjusting the potentiometers, IIN or FADJ. The modulation frequency was chosen based on the range of operation. We chose a 1-kHz modulation to enable operation at ranges up to 29m with a maximum beat frequency of 25 kHz and a sweep bandwidth of 130 MHz (from (8.3)).

#### 8.4.2 *FM Driver*

The center frequency of the YIG oscillator can be deviated as much as  $\pm 70$  MHz by pumping current into the FM coil. The sensitivity of the FM coil was given as 450 kHz/mA. To achieve a sweep bandwidth of 140 MHz we need as much as  $\pm 155.6$  mA, of current flowing into the FM coil. This is well within the maximum threshold of  $\pm 200$  mA specified by the manufacturer. The FM driver was first designed to produce a current of  $\pm 155.6$  mA but upon testing it with the spectrum analyzer, it was found that this amount only deviated the center frequency by  $\pm 55$  MHz. The current flow was then increased to  $\pm 190$  mA to deviate the center frequency by  $\pm 65$  MHz. Hence, a range resolution of 1.15 m is obtained for a sweep bandwidth of 130 MHz.

The figure below shows the circuit layout of the FM Driver.

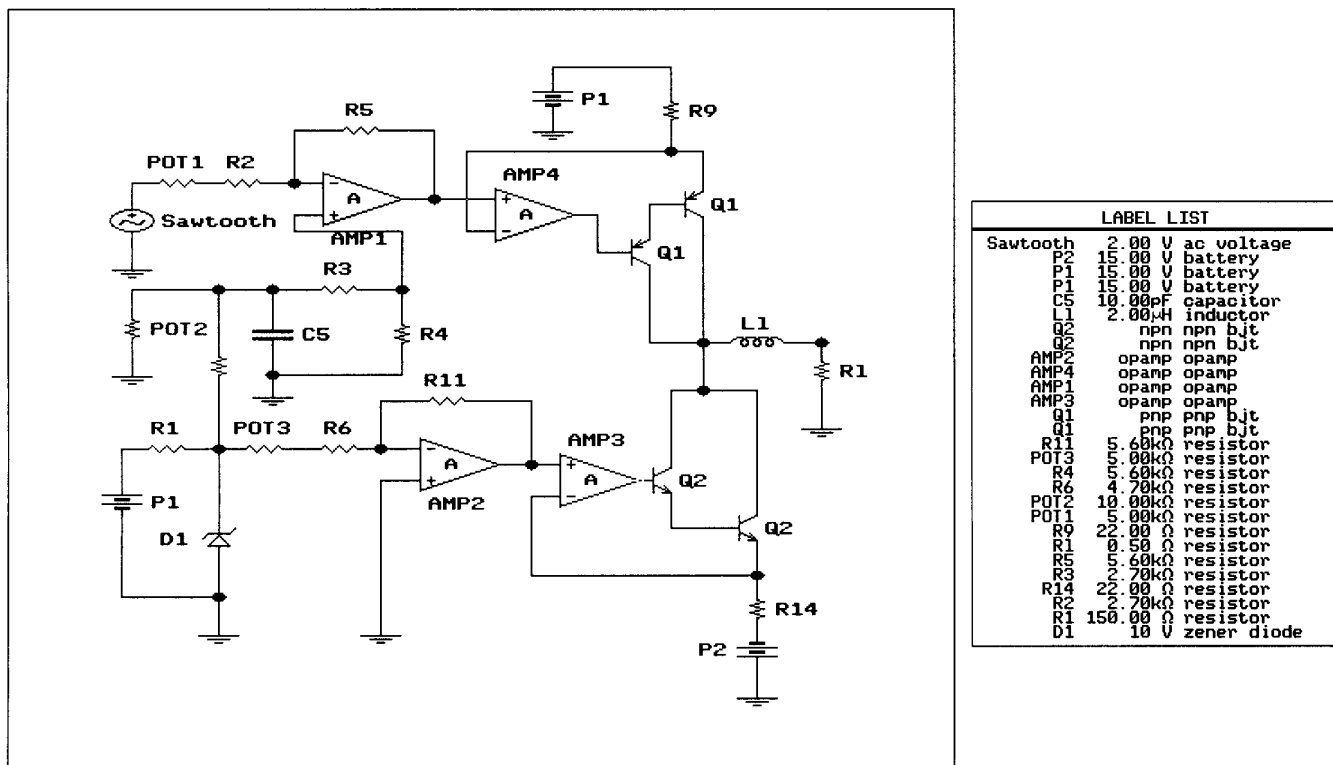


**Figure 8.8** Circuit layout of FM driver.

In the diagram above,  $R_1$  and  $L_1$  represent the input impedance of the FM port.  $Q_1$  is a PNP Darlington transistor that supplies current from 0 to 380 mA to the FM port.  $Q_1$  is designed to supply 380mA when the input voltage is +2V and 0mA when the input voltage is -2V. This is done by selecting the appropriate resistor values for  $R_2$  and  $R_5$  of the difference amplifier AMP1. The variable resistor, POT1, is used to fine tune the current range to be 380 mA. Thus, the bandwidth of the FM sweep can be adjusted using POT1. AMP4 acts as a buffer that drives  $Q_1$ . The voltage appearing

at the positive terminal of AMP1 can be adjusted with the variable resistor POT2 to offset the current to be exactly 0 to 380 mA. Hence, POT2 is an FM bandwidth offset adjuster. D1 is a 10V zener diode that provides a stable +10V supply. This voltage is used as a reference voltage for POT2 to set the offset voltage at the positive terminal of AMP1 and also as the input voltage to AMP2 for setting the reference voltage at  $R_{14}$ .

Q2 is a NPN Darlington transistor that pulls a constant +190 mA current out of the FM port. This effectively supplies +/- 190mA to the FM port. To achieve this, the voltage across the 22  $\Omega$  resistor ( $R_{14}$ ) was designed to be about 4.2 V. This would result in 190 mA of current in the emitter of Q2. Since the common-emitter current gain for the Darlington configuration is very large ( $\beta=2500$ ), the current in the collector of Q2 can also be assumed to be about 190 mA. Because of the large wattage (about 1W) generated across the resistors  $R_9$  and  $R_{14}$ , we chose 3W resistors to withstand the high wattage. The op-amp, AMP2, is an inverting amplifier that provides the reference voltage across the resistor  $R_{14}$ . The resistors  $R_6$  and  $R_{11}$  are chosen to obtain the required voltage at  $R_{14}$  and POT3 is a variable resistor that can be used to fine tune the reference voltage at  $R_{14}$ . AMP3 is a buffer that drives the base of Q2.

The circuit in figure 8.8 was simulated using the computer program, Electronics Workbench, to verify the operation of the FM driver. The results of the simulation are shown in figure 8.9. Figure 8.9 (a) shows the input triangle waveform, which goes from -2 V to +2 V and figure 8.9 (b) shows the output at the FM port,

which goes from -0.1 V to +0.1 V. This is effectively -200 mA to +200 mA across a 0.5  $\Omega$ .

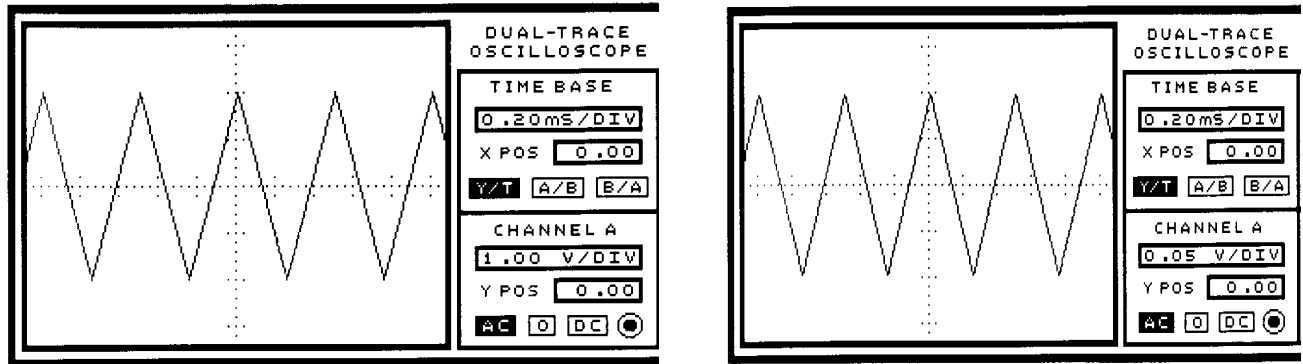


**Figure 8.9** (a) FM driver's input waveform. (b) FM driver's output waveform.

### 8.4.3 RF Section

The RF section of this radar operates in the 2- to 18-GHz frequency range. This section is responsible for transmitting and receiving the FM signal.

#### YIG Oscillator

A digital-tuned YIG oscillator was used as the signal source for the RF section. The center frequency was stepped by sending the control bits from the PC to the YIG's digital driver via a CIODIO-24 control board. There are 12 bits used to determine the center frequency with  $0_h$  and  $FFF_h$  corresponding to 2 and 18 GHz, respectively. Each bit corresponds to a frequency resolution of

$$\Delta f = \frac{(18 - 2)GHz}{(FFF_h - 0)} \quad (8.14)$$

$$\begin{aligned} &= \frac{16GHz}{4095} \\ &= 3.9072 MHz \end{aligned}$$

To determine the accuracy of the given frequency resolution, tests were performed on the YIG oscillator using a spectrum analyzer. The spectrum analyzer was controlled by a PC via a GPIB board, and the YIG oscillator was stepped through the entire 4096 frequencies. At each frequency, the output power from the test port of the dual-directional coupler and the actual frequency of the YIG oscillator were recorded. The graphs in Figures 8.10 and 8.11 show the actual frequency step size of the oscillator and the deviation of the frequencies from their straight-line fit at various times after the YIG was turned on.

Ideally, the plot on Figure 8.10 should have zero standard deviation but standard deviation on the order of 0.12MHz is observed. The standard deviation exhibited a slight drop with an increase in time. It can be observed from figure 8.11 that the deviation at the edges of the frequency span is fairly high and it decreases with time. This indicates that the temperature of the oscillator needs to be stabilized for optimum performance.

Results from simulations in section 8.3 show that the oscillator needs to be operated in the linear region in order to avoid aliasing of the signal. This is the reason we decided to operate the radar from 2.37 GHz to 17.65 GHz instead of from 2 to 18 GHz.

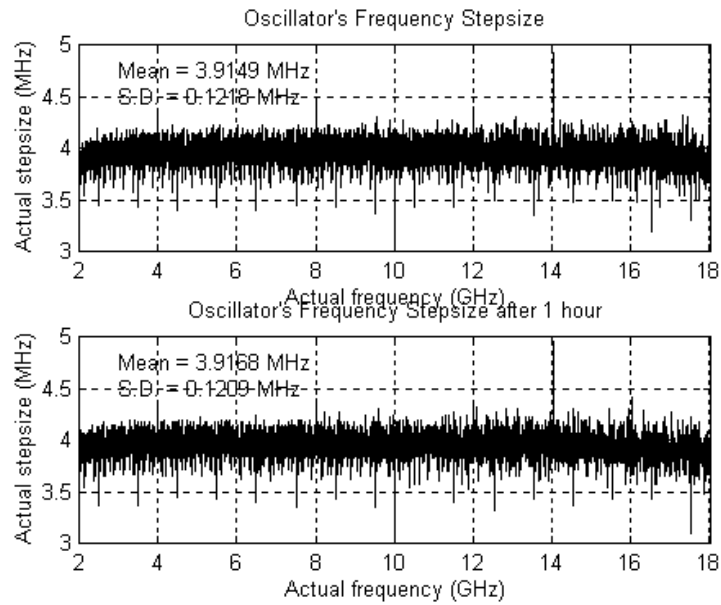


**Figure 8.10** Measured stepsize of oscillator's frequency.

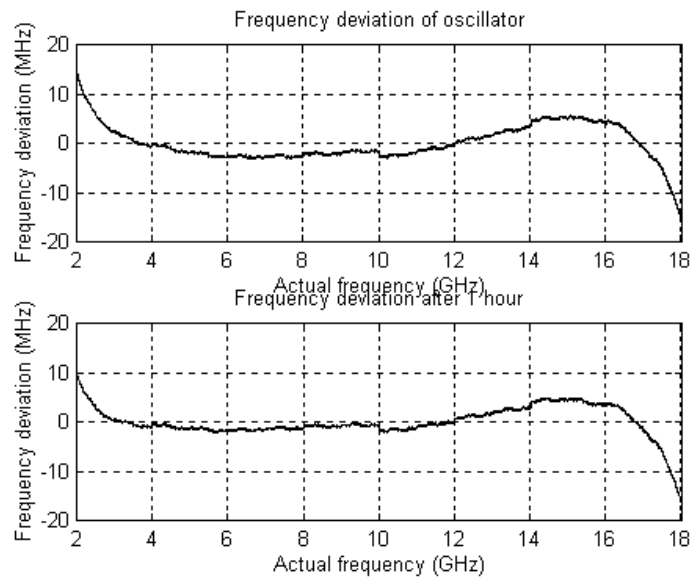


**Figure 8.11** Drift in oscillator's frequency.

### 6-dB Directional Coupler

The 6-dB directional coupler supplies one-fourth of the output power from the YIG oscillator to the LO port of the dual mixer for down converting the RF signal from the incident and reflected channels respectively. The remaining power is coupled to the input port of the dual-directional coupler.

### Dual-directional Coupler

For the dual-directional coupler we used an HP 772D. The input signal is derived from the 6-dB coupler. A fraction of this signal (-20 dB) is coupled to the test port for measurement, and the rest is coupled to the incident port. The signal from the incident channel is used as a calibration signal to remove system effects. This is achieved by matching the phase from the incident channel and reflected channel. This is done by placing a sub-delay line between the incident channel and the RF input of the dual mixer. The length of the sub-delay line was chosen to ensure that the returns from the incident channel and the reflected channel arrive at the same time at the input terminals of the dual mixer.

### Phase Trimmer

A phase trimmer is placed between the sub-delay line and the dual mixer to enable fine tuning the phase of the incident channel for matching to the reflected channel.

### Dual Mixer

The dual mixer is used to down convert the RF signal to IF on both the incident and reflected channels. The output from the YIG oscillator is used as the local oscillator (LO) to down convert the RF signal. The YIG's minimum output power is 15 dBm and one-fourth of 15 dBm is 9 dBm. Hence, for a LO power of 9dBm, the conversion loss for the dual mixer is 6.5 dBm.

### Coaxial Switch

The coaxial switch is used to enable us to make either single antenna ( $S_{11}$ ) or dual antenna ( $S_{21}$ ) radar measurements. The switch is driven by a 15 V source to switch between the  $S_{11}$  and  $S_{21}$  modes of operation.

#### 8.4.4 *IF Section*

The IF section is responsible for amplifying the down-converted RF signal coming from the dual mixer. The IF section consists of a 4-kHz high-pass filter and an IF amplifier.

The operation of the IF amplifier used in this radar has been documented [Lockhart, 1995]. A summary of that report is given here. Figure 8.12 shows the block diagram of the IF Section.

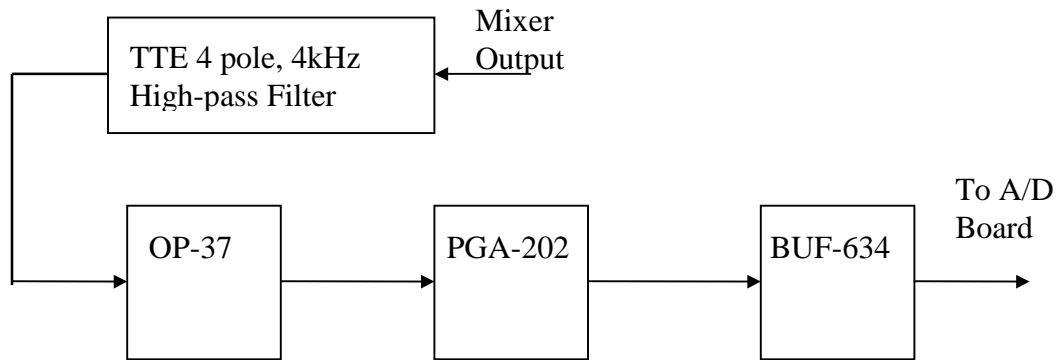


**Figure 8.12** Block diagram of IF section.

The RF signal, which has been down-converted by the mixer, is fed to a four-pole, 4-kHz high-pass filter to cut off leakage signals and reflection from the test port and the antenna. The output of the high-pass filter is then fed to the input of the IF amplifier. The IF amplifier consists of three stages to amplify the signal to the required gain level. The first stage is a single-pole high-pass filter with a fixed gain of 30 dB implemented with the OP-37 op-amp. The second stage is a programmable gain amplifier with gains of 0, 20, 40, and 60 dB. The gain of the amplifier is set by sending the appropriate gain bits from the computer to the PGA-202 chip via the CIODIO-24 I/O board. The final stage is a unity-gain buffer (BUF 634) used to boost the output current of the programmable gain amplifier to a level sufficient for driving a 50- $\Omega$  load.

#### 8.4.5 Data Acquisition

The data acquisition is performed by digitizing the IF signal at the output of the IF amplifier using a high-speed A/D board. We used the RTI-860 A/D board from Analog Devices to digitize the IF signal. The RTI-860 is capable of sampling at 250 kHz with 12-bit resolution in single-channel mode and up to 200 kHz in multi-channel mode. Sampling rates up to 330 kHz in single-channel mode and 250 kHz in multi-channel mode can be achieved using 8-bits of resolution. For N-bit resolution, the maximum SNR (signal-to-noise ratio) that can be measured is given by

$$SNR_{\max} \approx 6 \times (N - 1) - 1.25 \text{ (dB)} \quad (8.15)$$

Hence, for 8-bit resolution, the maximum SNR that can be measured is 40.75 dB and for 12-bit resolution it is 64.75 dB.

The input voltage range can be selected with a jumper to be either +/- 5V or +/- 10V. The digitized data can be stored in either the on-board memory or the system memory. The RTI-860 has 256K x 12 bits of dynamic RAM (DRAM) for storing the acquired data without being interrupted by the computer's CPU. Three methods of triggering A/D conversions with the RTI-860 are available. These are

##### 1) Digital signal triggering

Digital signal triggering is edge triggering by an external digital signal. The RTI-860 can be configured to trigger via software on either the falling edge or on the rising edge of the external digital signal.

## 2) Analog trigger

Analog triggering is done by comparing an external analog input signal with a software-specified threshold voltage. The RTI-860 can be configured via software to trigger when the analog signal is above or below the specified threshold voltage.

## 3) Software trigger

Software triggering starts the A/D conversion as soon as the user requests data.

For our radar/probe we selected a sampling rate of 200 kHz with 12-bit resolution in multi-channel mode, which is effectively 50 kHz per channel since we have four channels. The trigger mechanism is a rising-edge digital-signal trigger that is synchronized to the sawtooth waveform. The digitized data are first stored in the on-board DRAM and then transferred to the system memory. The data acquisition program has been written in C language and interfaced with MATLAB for the data processing.

The block diagram of the packaged system is shown in Figures 8.13 and 8.14.

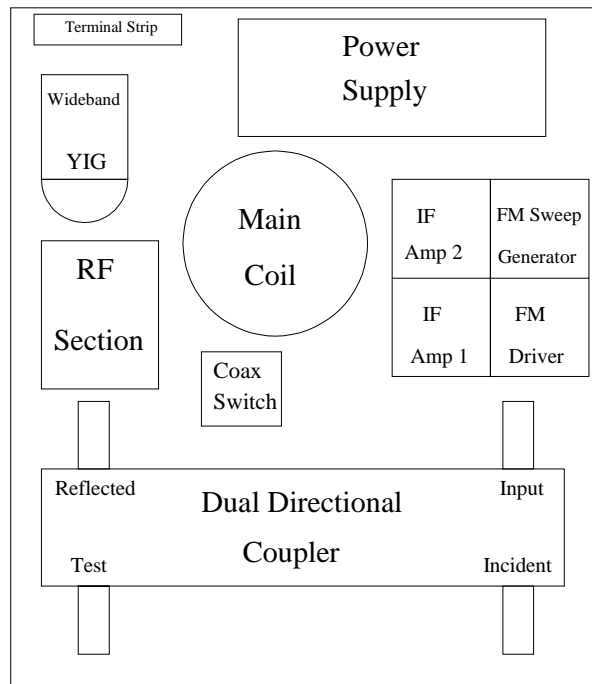


**Figure 8.13** Component layout of the range-gated step-frequency radar.

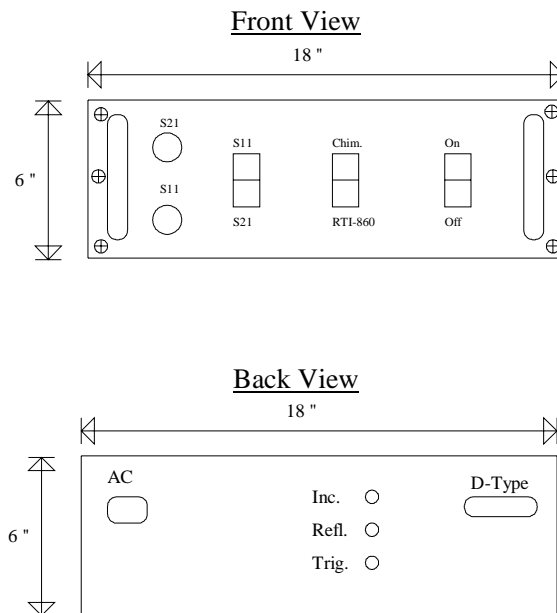


**Figure 8.14** Front and back panel of the radar/probe.

## 8.5 Systems Test

To test the system's ability to measure the relative permittivity of materials, we developed a cylindrical monopole antenna. To measure the relative permittivity of a material accurately, it is best that the material is disturbed as little as possible. The monopole antenna was chosen because of the ease in preparing the sample. Only one hole, the length of the antenna, needs to be drilled to be able to immerse the antenna into the medium. Figure 8.15 shows the configuration of the monopole antenna. To use existing models [Smith and Nordgard, 1985] to model the input impedance of the monopole antenna, we had to choose the antenna length ( $h$ ) and its diameter ( $d$ ) such that it resonates; viz, to make the input reactance zero. From the experiment done by Brown and Woodward [1945], we found that the ratio of length to diameter needs to be at least 10 in order to resonate. The length of the monopole antenna at the first resonant frequency is given by [Balanis, 1982],

$$h = \frac{0.24c}{f} - \frac{d}{2} \quad (8.16)$$

We calculated the length of the antenna to be 5 mm and the diameter to be 0.5 mm based on a resonant frequency of 14 GHz and an  $h/d$  ratio of 10. A larger ratio would be better in terms of modeling the input impedance but that would mean a smaller diameter and, hence, a thinner antenna. A thinner antenna is impractical because drilling narrow holes is difficult and the antenna can be easily broken. The measured and theoretical input impedance in free space calculated using the moment method are shown in figure 8.16.

The radiation efficiency of the antenna system is dependent on the ground plane of the antenna. In general, the radius of the ground plane should be at least a quarter wavelength at the lowest operating frequency [Collin, 1985]. Since our lowest operating frequency is 2 GHz, we constructed a ground plane with a diameter of 7.54 cm.

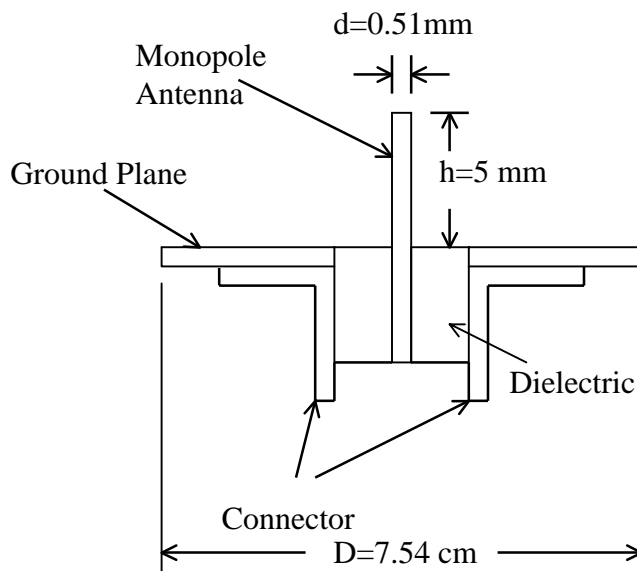


**Figure 8.15** Configuration of the monopole antenna.

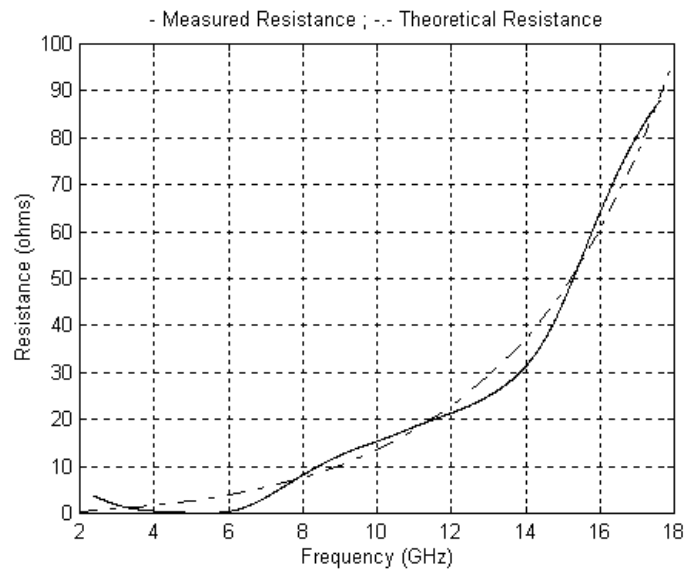


**Figure 8.16 (a)** Real part of input impedance.

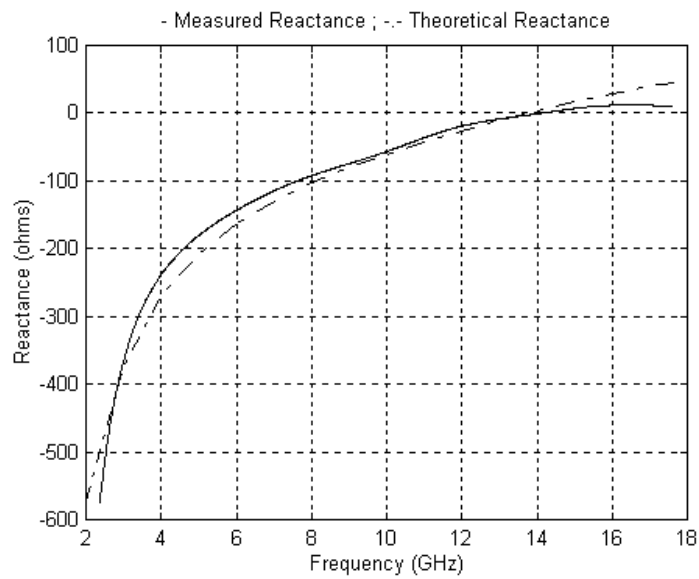


**Figure 8.16 (b)** Imaginary part of input impedance.

To measure the relative permittivity of materials using the monopole antenna, we need to determine the input impedance of the antenna in the measured medium. The relationship between the input impedance ( $Z$ ) of the antenna in a medium and the reflection coefficient ( $\Gamma$ ) of the medium is given by

$$Z(\omega, \epsilon) = Z_o \frac{1 + \Gamma(\omega, \epsilon)}{1 - \Gamma(\omega, \epsilon)} \quad (8.17)$$

where  $Z_o$  is the characteristic impedance of the line ( $50 \Omega$ ).

Deschamps' theorem [1962] states that for a short monopole antenna, the relationship between the input impedance of the antenna immersed in two mediums with different permittivity is

$$\sqrt{\epsilon_{r1}} Z_1(\omega_1, \epsilon_{r1}) = \sqrt{\epsilon_{r2}} Z_2(\omega_2, \epsilon_{r2}) \quad (8.18)$$

It has been shown by Smith and Nordgard [1985] that the input impedance of the antenna can be modeled in terms of the complex wave number,  $k$ , and the physical length of the antenna,  $h$ , by a rational function. The normalized input impedance is given as

$$\begin{aligned} Z_n(kh) &= \sqrt{\epsilon_r} Z(\omega, \epsilon_r) \\ &= \frac{kh}{k_o h} Z(\omega, \epsilon_r) \end{aligned} \quad (8.19)$$

where  $k_o$  is the wavenumber in free space ( $2\pi/\lambda$ ) and  $Z_n(kh)$  is the normalized input impedance that can be modeled by the following rational function of order  $m+1$ ,

$$Z_n(kh) \approx j \frac{K}{kh} \left[ \frac{1 + jb_1(kh) + b_2(kh)^2 + jb_3(kh)^3 + \dots + b_m(kh)^m}{1 + ja_1(kh) + a_2(kh)^2 + ja_3(kh)^3 + \dots + a_m(kh)^m} \right] \quad (8.20)$$

This model assumes antenna resonance, so we designed our antenna so that the ratio of the antenna length to the diameter would be greater than ten.

To determine the relative permittivity of materials the following procedure is used.

- 1) Measure input impedance of antenna in air.
- 2) These data are used to determine the coefficients in (8.20). For a rational function of order 3, an algebraic solution is given for the coefficients [Smith and Nordgard, 1985].
- 3) The input impedance is then measured in the material. From (8.18), solve for kh. The data are valid over the frequency range where  $|kh| \leq |k_0 h|_{\text{res}}$
- 4) The relative permittivity,  $\epsilon_r$ , is

$$\epsilon_r = \left( \frac{kh}{k_0 h} \right)^2 \quad (8.21)$$

The accuracy of the relative permittivity is dependent on the accuracy of the measurement of the reflection coefficient. To obtain accurate measurement of the reflection coefficient at the test port, we need to calibrate the system up to the point of measurement. Our calibration can be described by the equations below:

$$H(f) = \frac{-1}{S(f)} \quad (8.22)$$

$$\Gamma_M(f) = H(f) \times M(f) \quad (8.23)$$

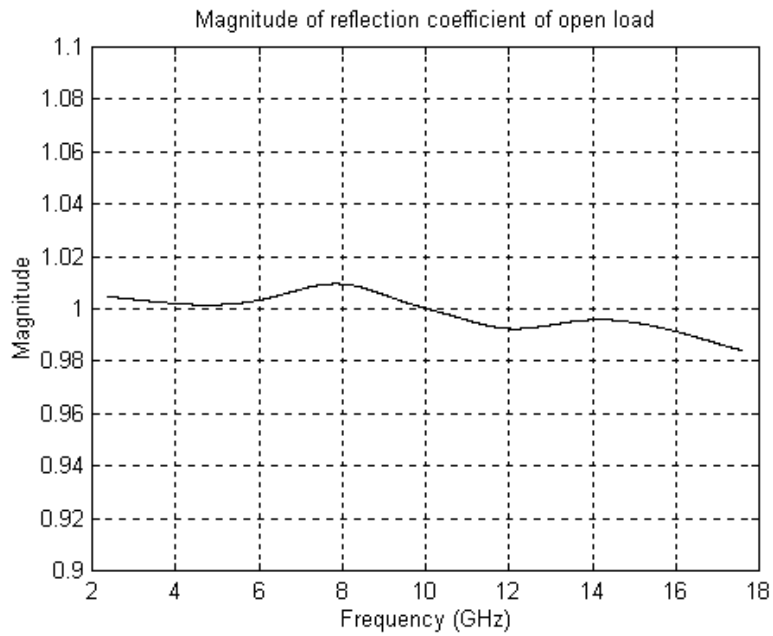
where  $S(f)$  is the measured reflection from the short circuit load,

$H(f)$  is the calibration factor,

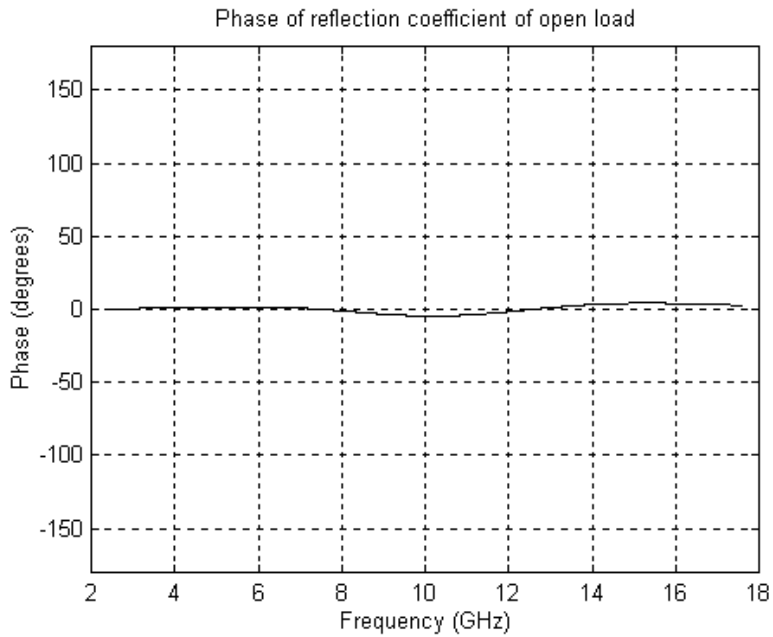
$M(f)$  is the measured reflection from the medium and

$\Gamma_M(f)$  is the true reflection from the medium.

We calibrated the system by measuring the reflection coefficient of the short circuit,  $S(f)$ , at the test point. The calibration factor,  $H(f)$ , is obtained by dividing the true reflection of the short circuit load, which is -1, by  $S(f)$ . This function,  $H(f)$ , is multiplied by the measured reflection from the medium to obtain the true reflection from the medium. Figure 8.17 shows the accuracy of our calibration technique. We obtained the reflection coefficient of an open load ( $\Gamma_{\text{open}}=1$ ) with less than 2% error in magnitude and less than 3% error in phase across the frequency range.

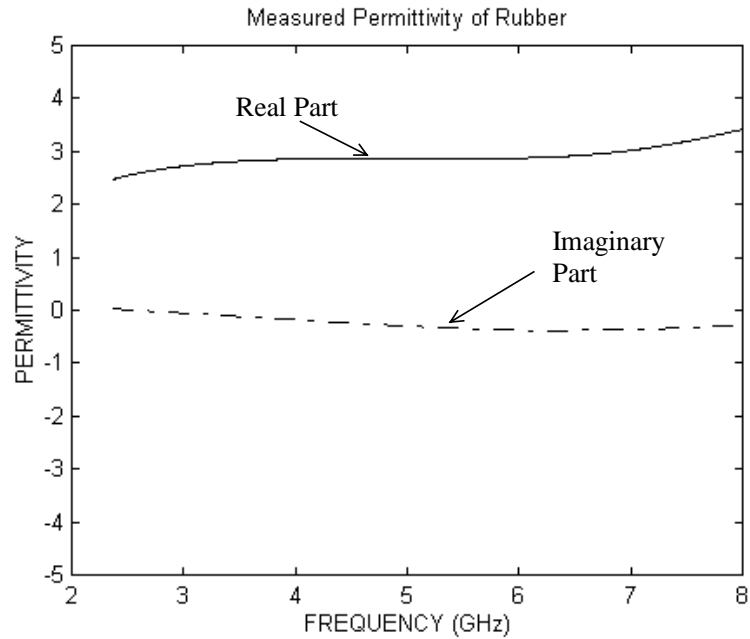


**Figure 8.17 (a)** Magnitude of reflection coefficient of open load.



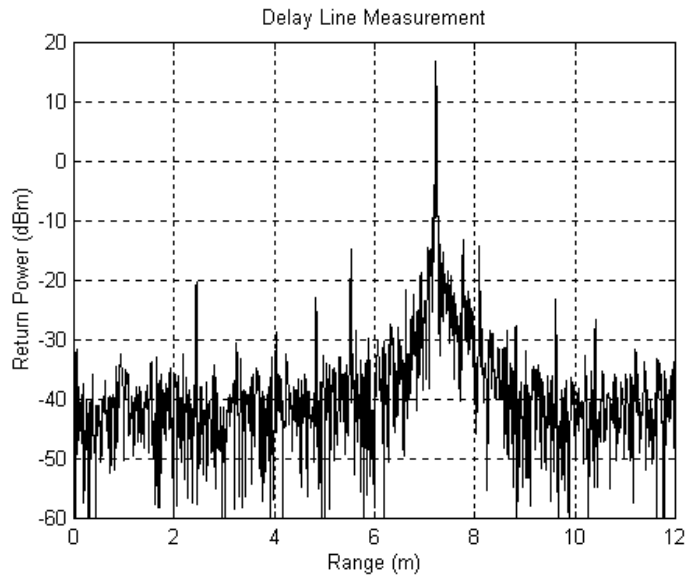
**Figure 8.17 (b)** Phase of reflection coefficient of open load.

Figure 8.18 shows the relative permittivity of rubber obtained using the monopole antenna. The theoretical relative permittivity is given as 3 for the real part and 0 for the imaginary part.



**Figure 8.18** Measured permittivity of rubber. Theoretical permittivity of rubber is 3 for the real part and 0 for the imaginary part.

Figure 8.19 shows the delay line measurement made in  $S_{21}$  mode.



**Figure 8.19** Result of delay line measurement with 0-dB gain.

## 8.6 Conclusions and Future Work

We have shown that the step-frequency radar can be operated using the FM-CW concept. Our radar has the FM-CW radar's unambiguous range with the resolution of a step-frequency radar. This radar can be operated in either single-antenna or dual-antenna mode. In CW step-frequency radars, range gating can only be done by implementing switches. To operate at short distances, the switching times need to be in the order of nanoseconds, and implementation of such switches are difficult. Range gating is easily implemented in our radar, using filters.

Previously, we needed a network analyzer for ultra-wideband operation. The network analyzer is not very practical for field measurements because of its size and weight. It is now possible to operate in ultra-wideband mode using our compact

system. Results of permittivity measurements of rubber using this system agree with theoretical results.

Performance of this radar can be further improved by linearizing the frequency steps by using a direct digital synthesizer (DDS). The IF spectrum can be further improved if the IF signal is weighted by a window before it is input into the range-gating filter to reduce the effects of ringing. The radar has a wide range of applications including high-resolution probing of geophysical surfaces and ground-penetration applications.

## REFERENCES

- Anderson, V.H., High altitude, side looking radar images of sea ice in the Arctic, *Proceedings of the Fourth Symposium on Remote Sensing of the Environment*, pp. 845-857, Willow Run Laboratory, Ann Arbor, Michigan, 1966.
- Balanis, C.A., *Antenna Theory Analysis and Design*, Harper & Row, New York, 1982.
- Beaven, S., Radar Backscatter Measurements from Simulated Sea Ice and Arctic Sea Ice during the Fall Freeze-up, MS Thesis, University of Kansas, 1992.
- Beaven, S., and S.P. Gogineni, Shipborne radar backscatter measurements from Arctic sea ice during the fall freeze-up, *Remote Sensing Reviews*, vol. 9, nos. 1-2, pp. 3-25, 1994.
- Beaven, S., Sea Ice Radar Backscatter Modeling, Measurements, and the Fusion of Active and Passive Microwave Data, Ph.D. Dissertation, University of Kansas, 1995.
- Brown, G.H., and O.M. Woodward, Jr., Experimentally Determined Impedance Characteristics of Cylindrical Antennas, *Proceedings of the IRE*, pp. 257-262, April 1945.
- Carsey, F.D., R.G. Barry, and W.W. Weeks, Introduction, in *Microwave Remote Sensing of Sea Ice*, edited by F.D. Carsey (Washington DC, American Geophysical Union), Geophysical Monograph, vol. 68, pp. 1-7, 1992.

- Chakrabarti, S., Private Communication, Lawrence, KS, 1995.
- Collin, R.E., *Antennas and Radiowave Propagation*, McGraw-Hill, New York, 1985.
- Drinkwater, M.R., R. Hosseinmostofa and S.P. Gogineni, C-band backscatter measurements of winter sea ice on the Weddell Sea, Antarctica, *International Journal of Remote Sensing*, vol. 16, no. 17, pp. 3365-3389, 1995.
- Deschamps, G.A., Impedance of an antenna in a conducting medium, *IRE Transactions on Antennas and Propagation*, pp. 648-650, September 1962.
- Gogineni, S.P., Radar Backscatter from Summer and Ridged Sea Ice, and the Design of Short-Range Radars, Ph.D. Dissertation, University of Kansas, 1984.
- Gogineni, S.P., K. Jezek, L. Peters, J. Young, S. Beaven, and E. Nassar, Application of plane waves for accurate measurement of microwave scattering from geophysical surfaces, *IEEE Transactions on Geoscience and Remote Sensing*, vol. 33, no. 3, pp. 627-633, 1995.
- Gray, A.L., R.O. Ramseier, and W.J. Campbell, Scatterometer and SLAR results obtained over Arctic sea ice and their relevance to the problem of Arctic ice reconnaissance, *Proceedings of the Fourth Canadian Symposium on Remote Sensing*, pp. 423-443, 1977.
- Higgins, R.J., *Digital Signal Processing in VLSI*, Prentice Hall, Englewood Cliffs, New Jersey, 1990.

- Izuka, K., A.P. Freundorfer, K.H. Wu, H. Mori, H. Ogura, and V.K. Nguyen, Step-frequency radar, *Journal of Applied Physics*, vol. 56, no. 9, pp. 2572-2583, 1984.
- Jezek, K., S.P. Gogineni, L. Peters, J. Young, S. Beaven, E. Nassar, and I. Zabel, Microwave scattering from saline ice using plane wave illumination, *Digest IGARSS'94*, pp. 493-495, Pasadena, California, August 8-12, 1994.
- Kim, Y.S., Theoretical and Experimental Study of Radar Backscatter from Sea Ice, Ph.D. Dissertation, University of Kansas, 1984.
- Kouyoumjian, R.G., and P.H. Pathak, A uniform geometrical theory of diffraction for an edge in a perfectly conducting surface, *Proceedings of the IEEE*, vol. 62, pp. 1448-1461, Nov. 1974.
- Livingstone, C.E., K.P. Singh, and A.L. Gray, Seasonal and regional variations of active/passive microwave signatures of sea ice, *IEEE Transactions on Geoscience and Remote Sensing*, vol. GE-25, pp. 159-173, 1987.
- Lockhart, G.L., Development of an L-, C-, and X-Band Radar for Backscattering Studies over Vegetation, MS Project, University of Kansas, 1995.
- Maxim Integrated Products, High-Frequency Waveform Generator (MAX038), Data Sheet 19-0266; Rev 0; 6/94, 120 San Gabriel Drive, Sunnyvale CA 94086, 1994.
- Nassar, E.M., Aperture Distributions Generated by Transmission Line Feed Structures, MS Thesis, The Ohio State University, 1992.

- Onstott, R.G., and S.P. Gogineni, Active microwave measurements of Arctic sea ice under summer conditions, *Journal of Geophysical Research*, vol. 90, no. C3, pp. 5035-5044, 1985.
- Onstott, R.G., T.C. Grenfell, C. Mätzler, C.A. Luther, and E.A. Svendsen, Evolution of microwave sea ice signatures during early summer and midsummer in the marginal ice zone, *Journal of Geophysical Research*, vol. 92, no. C7, pp. 6825-6835, 1987.
- Onstott, R.G. and R.A. Shuchman, Comparison of SAR and scatterometer data collected during CEAREX, *Digest IGARSS'90 Symposium*, pp. 1513-1516, College Park, Maryland, 1990.
- Onstott, R.G., SAR and scatterometer signatures of sea ice, in *Microwave Remote Sensing of Sea Ice*, edited by F.D. Carsey (Washington DC, American Geophysical Union), Geophysical Monograph, vol. 68, pp. 73-104, 1992.
- Parashar, S.K., R.M. Haralick, R.K. Moore, and A.W. Biggs, Radar scatterometer discrimination of sea ice types, *IEEE Transactions on Geoscience and Electronics*, vol. GE-15, pp. 83-87, 1977.
- Pistorius, C., and W.D. Burnside, An improved main reflector design for compact range application, *IEEE Transactions on Antennas and Propagation*, vol. AP-35, pp. 342-346, Mar. 1987.
- Rouse, J.W., Arctic ice type identification by radar, *Proceedings of the IEEE*, vol. 57, no. 4, pp. 605-611, 1969.

Ryan, C.E., Jr., and L. Peters, Jr., Evaluation of edge-diffracted fields including equivalent currents for caustic regions, *IEEE Transactions on Antennas and Propagation*, vol. AP-17, pp. 292-299, May 1969.

Smith, G.S., and J.D. Nordgard, Measurement of the electrical constitutive parameters of materials using antennas, *IEEE Transactions on Antennas and Propagation*, vol. AP-33, no. 7, pp. 783-792, July 1985.

## **BIBLIOGRAPHY**

Balanis, C.A., *Advanced Engineering Eletromagnetics*, Wiley, New York, 1989.

Collin, R.E., *Foundations for Microwave Engineering*, McGraw-Hill, New York, 1966.

Hallikainen, M., and D.P. Winebrenner, The physical basis for sea ice remote sensing, in *Microwave Remote Sensing of Sea Ice*, edited by F.D. Carsey (Washington DC, American Geophysical Union), Geophysical Monograph, vol. 68, pp. 29-46, 1992.

HP 8719C, HP 8720C, HP 8722A/C Network Analyzer *Operating Manual*, Hewlett-Packard Company, Santa Rosa, California, 1991.

Ma, H., Development of Instrumentation for Measuring Dielectric Constant of Sea Ice, MS Thesis, University of Kansas, 1991.

Skolnik, M.I., *Introduction to Radar Systems*, McGraw-Hill, Singapore, 1981.

Ulaby, F.T., R.K. Moore, and A.K. Fung, *Microwave Remote Sensing: Active and Passive*, vol. I, Artech House, Norwood, Massachusetts, 1981.

Ulaby, F.T., R.K. Moore, and A.K. Fung, *Microwave Remote Sensing: Active and Passive*, vol. II, Artech House, Norwood, Massachusetts, 1982.

Ulaby, F.T., R.K. Moore, and A.K. Fung, *Microwave Remote Sensing: Active and Passive*, vol. III, Artech House, Norwood, Massachusetts, 1985.